23
Modeling Issues in Zeolite Applications

Rajamani Krishna
University of Amsterdam, Amsterdam, The Netherlands

I. INTRODUCTION

Zeolitic materials are used as sorbents and catalysts in a variety of processes within the chemical, petroleum, petrochemical, and food industries. Zeolite crystals are incorporated into binders (such as amorphous aluminosilicate) and perhaps a diluent (typically a clay mineral), and used in the form of powder (in fluidized beds) or pellets (in fixed beds). Alternatively, zeolite crystals are coated onto a porous membrane support and used in (catalytic) membrane permeation devices.

Zeolite-based processes are carried out either under steady-state, unsteady-state, or cyclic conditions. Fixed-bed adsorbers are typically operated under transient conditions. Zeolite membrane processes typically operate under steady-state conditions. Simulated moving-bed adsorbers operate under cyclic conditions. While many of the transport issues can be understood from the standpoint of classical diffusion and flow, special attention needs to be paid to the proper description of mixture sorption and diffusion in zeolites. The purpose of this chapter is to highlight the special features of zeolite sorption and diffusion by means of several illustrative examples of practical importance.

II. TRANSIENT UPTAKE OF A SINGLE COMPONENT WITHIN A ZEOLITE

Let us begin by considering the case of a batch adsorber in which zeolite particles are brought into contact with a fluid phase containing a component species i that diffuses into the particle (of diameter d_p) into which the zeolite crystals are embedded; see Fig. 1. There are three steps in the intraparticle diffusion process.

1. Component i in the bulk fluid phase surrounding the particle has first to diffuse across the stagnant layer, of thickness δ_f, surrounding the particle. The stagnant "film" thickness δ_f is determined by the fluid–particle hydrodynamics. Higher Reynolds numbers will lead to smaller δ_f values and, consequently, lower film diffusion resistance.

2. Next, component i diffuses into the *macro*pores. For a fluid at least four resistances contribute to transport in the macropore. These are *Knudsen diffusion* (a transport process when the fluid is essentially gaseous in nature, where molecular collisions between the diffusing species and the pore walls predominate); *surface diffusion* (diffusive motion of adsorbed species over the
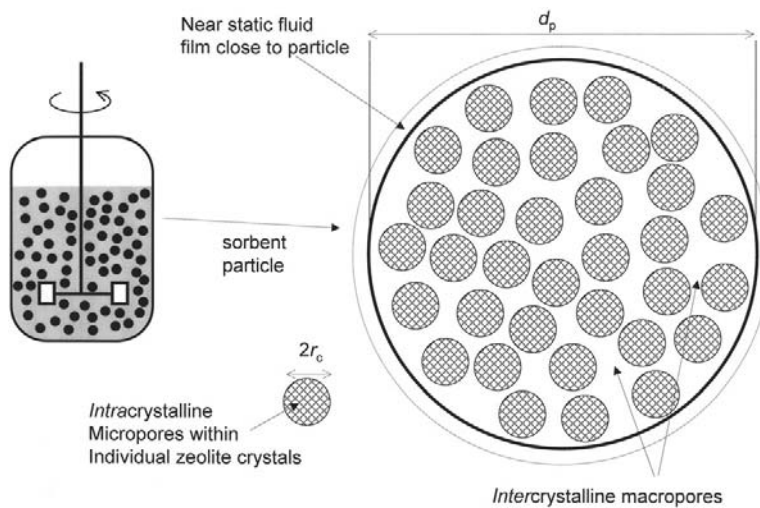
Fig. 1 Schematic showing a batch adsorber in which the (spherical) zeolite sorbent particles are exposed to a well-mixed fluid environment.

walls of the pores); *bulk diffusion* (a molecular transport process mediated primarily by collisions between the diffusing species themselves); and *viscous flow* (species convected by laminar flow down a pressure gradient inside the pore). With liquids in macropores only bulk and surface diffusion can be expected to make significant contributions to the effective macropore diffusivity.

3. Finally, component *i* diffuses inside the zeolite crystallites (assumed to be spherical with radius r_c). This diffusion process is termed intracrystalline or *micro*pore diffusion, and is also the focus of Chapter 10 in this volume.

We focus attention on the situation where intracrystalline diffusion is the "controlling" resistance. The reader is referred to standard texts of Ruthven (1–4), Yang (5), Do (6), and Chen et al. (7) for more detailed discussions of modeling macropore diffusion and external transport. The transient uptake within the zeolite crystallites is described by the following partial differential equation:

$$\frac{\partial q_i}{\partial t} = -\frac{1}{\rho}\frac{1}{r^2}\frac{\partial}{\partial r}(r^2 N_i) \tag{1}$$

where q_i is the molar loading of species *i*, expressed as moles adsorbed per kg of zeolite; N_i is the molar flux, expressed as mol/m^2/s; r is the radial distance coordinate; ρ is the zeolite density expressed in kg/m^3. Alternatively, we may express the loading as the number of molecules per unit cell Θ_i:

$$\frac{\partial \Theta_i}{\partial t} = -\frac{1}{\rho}\frac{1}{r^2}\frac{\partial}{\partial r}(r^2 N_i) \tag{2}$$

In this case, the density ρ is expressed as the number of unit cells per m^3 and the flux N_i as molecules/m^2/s. For MFI zeolite, for example a loading of four molecules per unit cell corresponds to 0.6935 mol/kg.

For the solution of Eq. (1) or (2), we need a constitutive equation for the flux N_i.

A. Fick, Onsager, and Maxwell-Stefan Approaches

The molar flux is commonly taken to be proportional to the gradient of the component loading:

$$N_i = -\rho D_i \frac{\partial q_i}{\partial r} = -\rho q_{i,sat} D_i \frac{\partial \theta_i}{\partial r} = -\rho \Theta_{i,sat} D_i \frac{\partial \theta_i}{\partial r} \tag{3}$$

where D_i is the Fick, or transport, diffusivity of species i; $q_{i,\text{sat}}$ and $\Theta_{i,\text{sat}}$ are the saturation loadings of species i; θ_i is the fractional occupancy, which obeys:

$$\theta_i = \frac{q_i}{q_{i,sat}} = \frac{\Theta_i}{\Theta_{i,sat}} \tag{4}$$

An alternative to the Fick formulation is the Onsager approach of irreversible thermodyamics; in this approach, the chemical potential gradients are recognized as the "proper" driving forces for diffusion:

$$N_i = \rho \Theta_{i,sat} L_i \frac{1}{RT} \frac{\partial \mu_i}{\partial r} \tag{5}$$

where R is the gas constant; T is the temperature; L_i is the Onsager coefficient; μ_i is the chemical potential of sorbed species i. Assuming (local) equilibrium between the sorbed species and the bulk fluid phase, we have the following relationship for the chemical potential μ_i:

$$\mu_i = \mu_i^o + RT \ln(f_i) \tag{6}$$

where μ_i^0 is the chemical potential in the chosen standard state and f_i is the fugacity. The chemical potential gradients may be expressed in terms of the occupancy gradient:

$$\frac{1}{RT} \frac{\partial \mu_i}{\partial r} = \frac{1}{\theta_i} \Gamma \frac{\partial \theta_i}{\partial r}; \quad \Gamma \equiv \theta_i \frac{\partial \ln f_i}{\partial \theta_i} \tag{7}$$

where Γ is the thermodynamic "correction" factor. If the bulk fluid phase is gaseous and the system pressures are not too high, the component partial pressure, p_i, can be used in place of the component fugacity, f_i, i.e. $f_i \approx p_i$.

The interrelation between the Fick and Onsager coefficient is

$$\frac{L_i}{\theta_i} = \frac{D_i}{\Gamma} \equiv Đ_i \tag{8}$$

Experimental data for several systems show that $Đ_i \equiv D_i/\Gamma$ is practically independent of the loading; this coefficient is referred to as the "corrected" or "jump" diffusivity. The corrected diffusivity $Đ_i$ is also identical to diffusivity that arises from the Maxwell-Stefan description of zeolite diffusion, to be developed below. As discussed in Chapter 10 in this volume, for strong confinement of guest molecules in zeolites, the Maxwell-Stefan diffusivity often decreases with loading, following a $Đ_i(0)(1-\theta_i)$ where $Đ_i(0)$ is the zero-loading diffusivity of the pure component.

Consider the sorption data for benzene in MFI at a temperature $T = 343$ K (8); cf. Fig. 2a. The experimental data are reasonably well represented by the Langmuir isotherm:

$$\Theta_i = \frac{\Theta_{i,sat} b_i P}{1 + b_i P}; \quad \theta_i = \frac{b_i P}{1 + b_i P} \tag{9}$$
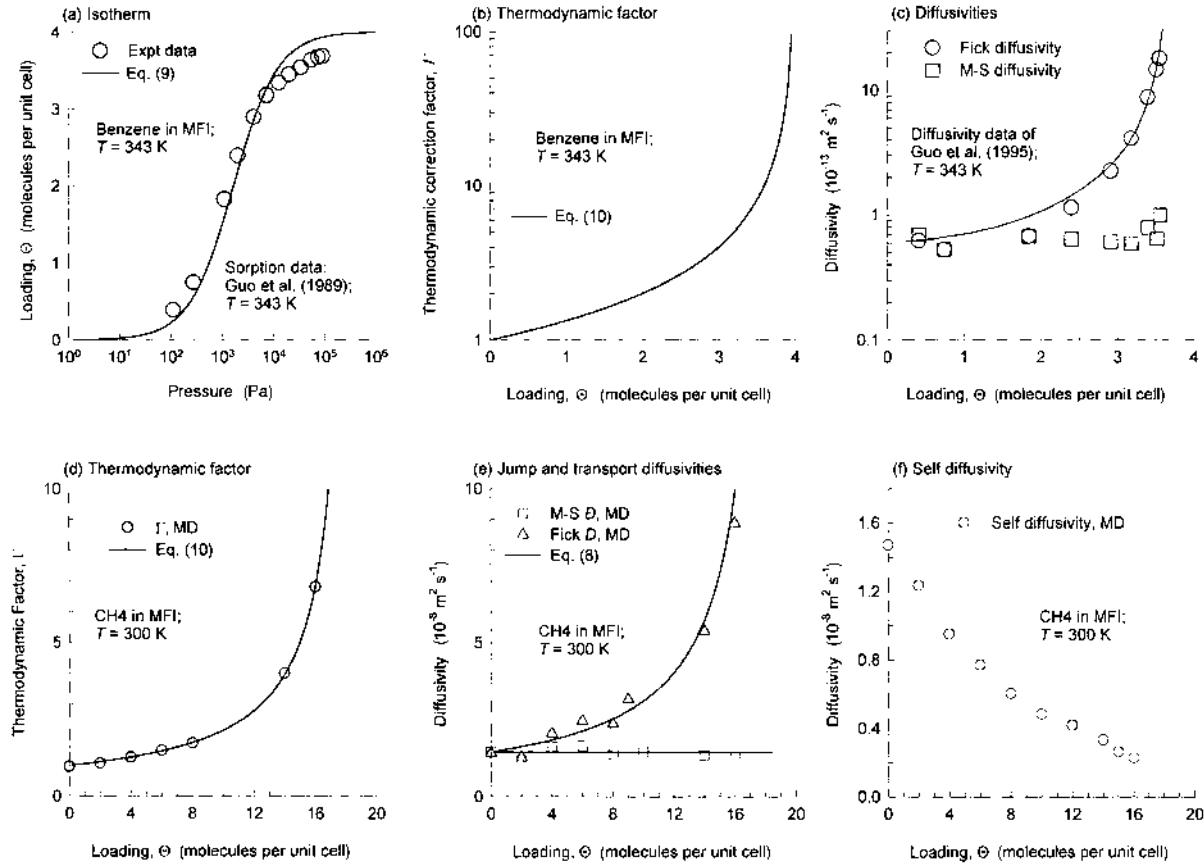
Fig. 2 (a) Pure component isotherms for sorption of benzene on MFI at a temperature of 343 K. (Experimental data from Ref. 8.) The Langmuir model parameters are $\Theta_{1,sat} = 4$, $b_{1,A} = 6 \times 10^{-4}$ Pa^{-1}. (b) The thermodynamic correction factor calculated using the Langmuir model. (c) Fick and Maxwell-Stefan diffusivity data for benzene in MFI at 343 K. (Data from Ref. 9). Molecular dynamics simulations of (d) thermodynamic factor, (e) jump and transport, and (f) self-diffusivities of CH$_4$ in MFI at 300 K. (MD data from Ref. 10.)

where the saturation capacity $\Theta_{i,\text{sat}}$ is four molecules per unit cell of MFI and the Langmuir constant $b_i = 6 \times 10^{-4}$ Pa^{-1}. The thermodynamic correction factor can be determined from Eq. (7) as follows:

$$\Gamma = \frac{1}{1-\Theta_i/\Theta_{i,sat}} = \frac{1}{1-\theta_i} \tag{10}$$

Figure 2b shows the variation of the thermodynamic factor with molecular loading. Notice the sharp increase in Γ as Θ_i approaches the saturation capacity, $\Theta_{i,\text{sat}}$ (=4). The Fick diffusivity data for benzene in MFI measured by Shah et al. (9) are shown in Fig. 2c and are seen to parallel the behavior of Γ. As seen in Fig. 2c D_i increases sharply as Θ_i approaches the saturation capacity, $\Theta_{i,\text{sat}}$ (=4). The Maxwell-Stefan diffusivity $Đ_i$ is practically independent of the sorbate loading; see the square symbols in Fig. 2c.

Consider now the Molecular Dynamics (MD) simulation results of Maginn et al. (10) for diffusion of CH_4 in MFI at 300 K for Γ, $Đ$, and D that have been reproduced in Fig. 2d and e. The simulated Γ follows Langmuirian behavior with a fitted value of $\Theta_{\text{sat}} = 18.76$ molecules per unit cell; see Fig. 2d. From Fig. 2e, we note that the jump, or Maxwell-Stefan diffusivity, is essentially independent of loading. The transport D, which is the product, $Đ\Gamma$, shows the same trend as does Γ; see Fig. 2b. The MD simulations for the self-diffusivity D^* show that these decrease with loading; this is due to vacancy correlation effects as discussed by Paschek and Krishna (11). The self-diffusivity cannot be identified with the jump diffusivity except at zero loadings.

B. Adsorption vs. Desorption Rates

An important consequence of the nonlinear loading dependence of the Fick diffusivity following $D_i = Đ_i/(1-\theta_i)$ is that *ad*sorption and *de*sorption processes do not proceed at the same rate. During the adsorption process the Fick diffusivity increases with time, i.e., with loading. Conversely, during the desorption process the Fick diffusivity decreases with time and therefore proceeds considerably more slowly than adsorption. This asymmetry is illustrated by calculations for diffusion of ethane in 4A zeolite presented in Fig. 3, which were obtained by solving the partial differential Eq. (1) subject to the following conditions:

$$\text{Initial condition: } t = 0; \quad 0 < r < r_c: \quad q_i = q_{i,0}; \quad \Theta_i = \Theta_{i,0}; \quad \theta_i = \theta_{i,0} \tag{11}$$

$$\text{Boundary (surface) condition: } t > 0; \quad r = r_c: \quad q_i = q_{i,s}; \quad \Theta_i = \Theta_{i,s}; \quad \theta_i = \theta_{i,s} \tag{12}$$

Here $q_{i,0}$ is the initial loading and $q_{i,s}$ is the loading that is in equilibrium with the bulk fluid phase. The Maxwell-Stefan diffusivity of ethane 4A zeolite is taken as $Đ_i/r_c^2 = 2.45 \times 10^{-4}$ s^{-1} following Garg and Ruthven (12). The method of lines (13) was used to solve the set of Eqs. (1), (3), and (10). The y axis in Fig. 2 represents the fractional approach to equilibrium, defined as $(\bar{q}_i - q_{i,0})/(q_{i,s} - q_{i,0})$ where $\bar{q}_i$ is the average loading within the particle at any time t, defined by

$$\bar{q}_i = \frac{3}{r_c^3} \int_0^c q_i r^2 dr \tag{13}$$

As can be seen in Fig. 3, there is excellent agreement between the experiments of Garg and Ruthven (12) and the simulation results. Also, the results shown in Fig. 3 confirm the asymmetry in adsorption and desorption kinetics.
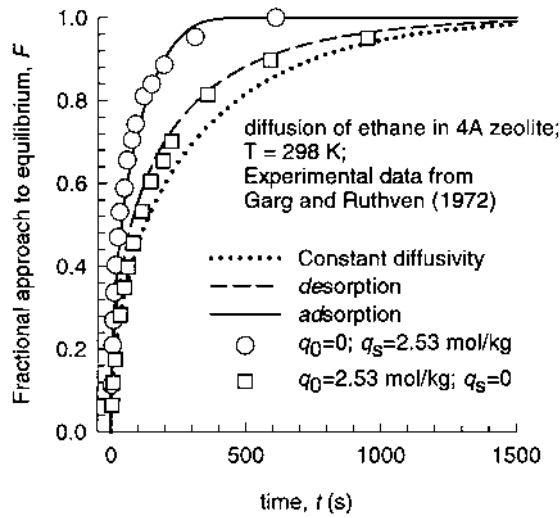
Fig. 3 Adsorption and desorption of ethane in 4A zeolite. (Experimental data from Ref. 12.) The simulation results with $Đ_i/r_c^2 = 2.45 \times 10^{-4}$ s^{-1}.

C. Constant Fick Diffusivity and LDF Models

If the Fick diffusivity is independent of the loading, Eq. (1) can be solved analytically to obtain

$$\frac{(\overline{q}_i - q_{i,0})}{(q_{i,s} - q_{i,0})} \equiv F = 1 - \frac{6}{\pi^2} \sum_{m=1}^{\infty} \frac{\exp\left(-m^2 \pi^2 \frac{D_i}{r_c^2} t\right)}{m^2} \tag{14}$$

For comparison purposes, this constant-D solution is also plotted in Fig. 3 with a dotted line. It is clear that thermodynamic correction factor, given by Eq. (10), has a significant influence on adsorption and desorption rates.

Equation (14) can be used to obtain the time-averaged Sherwood number (Sh) within the zeolite crystals:

$$Sh \equiv \frac{k(2r_c)}{D} \equiv -\frac{2}{3\left(\frac{D_i}{r_c^2} t\right)} \ln(1 - F) \tag{15}$$

where F is the fractional approach to equilibrium given by Eq. (14), and k in Eq. (15) is defined by the second equality. The variation of the Sh and F with the Fourier number, tD/r_c^2, is shown in Fig. 4. In the adsorption literature a constant value of $Sh = 10$, corresponding to a 75% approach to equilibrium, is usually taken to model uptake in batch adsorbers and breakthrough curves in packed beds. This assumption is usually referred to as the linear driving force (LDF) approximation. In general, the LDF approach is not appropriate for modeling of zeolitic adsorption because of the strong dependence of the Fick diffusivity on the loading. The LDF approach is probably good enough when the fractional loading θ in the zeolite is below about 0.2 during the entire process. For such cases, the constant-D assumption may be justified. For all other cases, we have to contend
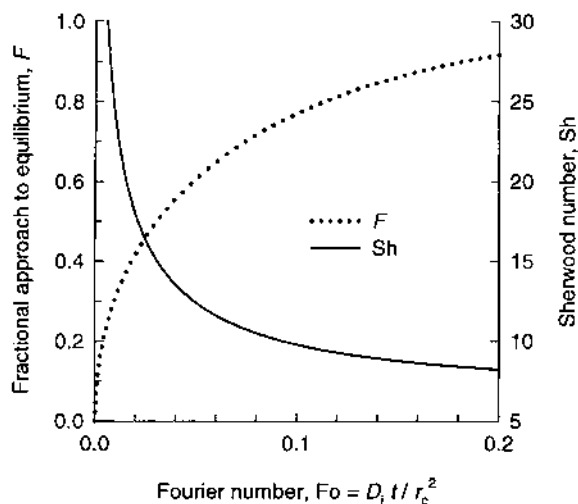
Fig. 4 Simulation of intraparticle diffusion using constant diffusivity model.

with solving the nonlinear partial differential equations (1) within the zeolite crystal. We do not discuss the LDF approximation further in this chapter and refer the reader to standard texts (1–6).

D. Isotherm Inflection Influence

In the foregoing discussions we have used the Langmuir isotherm to describe the sorption isotherm; in many cases the isotherms exhibit inflection behavior. Configurational bias Monte Carlo (CBMC) simulations of the isotherms of alkanes in the one- to seven-carbon-atom range at 300 K in MFI zeolite are shown in Fig. 5; the CBMC simulation technique has been described in detail in publications by Smit and coworkers (14–21) (see also Chapter 9 in this volume by the same authors). Normal heptane shows a pronounced inflection at a loading of $\Theta = 4$. Normal hexane shows a slight inflection at this loading due to "commensurate freezing" effects (22). All 2-methylalkanes show inflection behavior (see Fig. 5c); this is because these molecules prefer to locate at the intersections between straight and zig-zag channels, which offers more "leg room" (20). At $\Theta = 4$ all intersections are fully occupied. To locate the 2-methylalkanes within the channel interiors requires an extra push, leading to inflection behavior. The 2,2-dimethylbutane (22DMB) and 2,2-dimethylpentane (22DMP) molecules are too bulky to be located at the channel interiors, and both molecules show a maximal (saturation) loading of 4 (see Fig. 5d).

A simple model accounting for inflection behavior is the dual-site Langmuir (DSL) model. In this model the loading, $\Theta_i^0(P)$, expressed in molecules per unit cell, is expressed as a function of the pressure P as follows:

$$\Theta_i^0 \equiv \Theta_{i,A} + \Theta_{i,B} = \frac{\Theta_{i,sat,A}b_{i,A}P}{1 + b_{i,A}P} + \frac{\Theta_{i,sat,B}b_{i,B}P}{1 + b_{i,B}P} \tag{16}$$

The superscript 0 on $\Theta_i^0(P)$ is used to emphasize that the relation is for *pure* component loadings. In Eq. (16), $b_{1,A}$ and $b_{1,B}$ represent the DSL model parameters expressed in Pa^{-1}
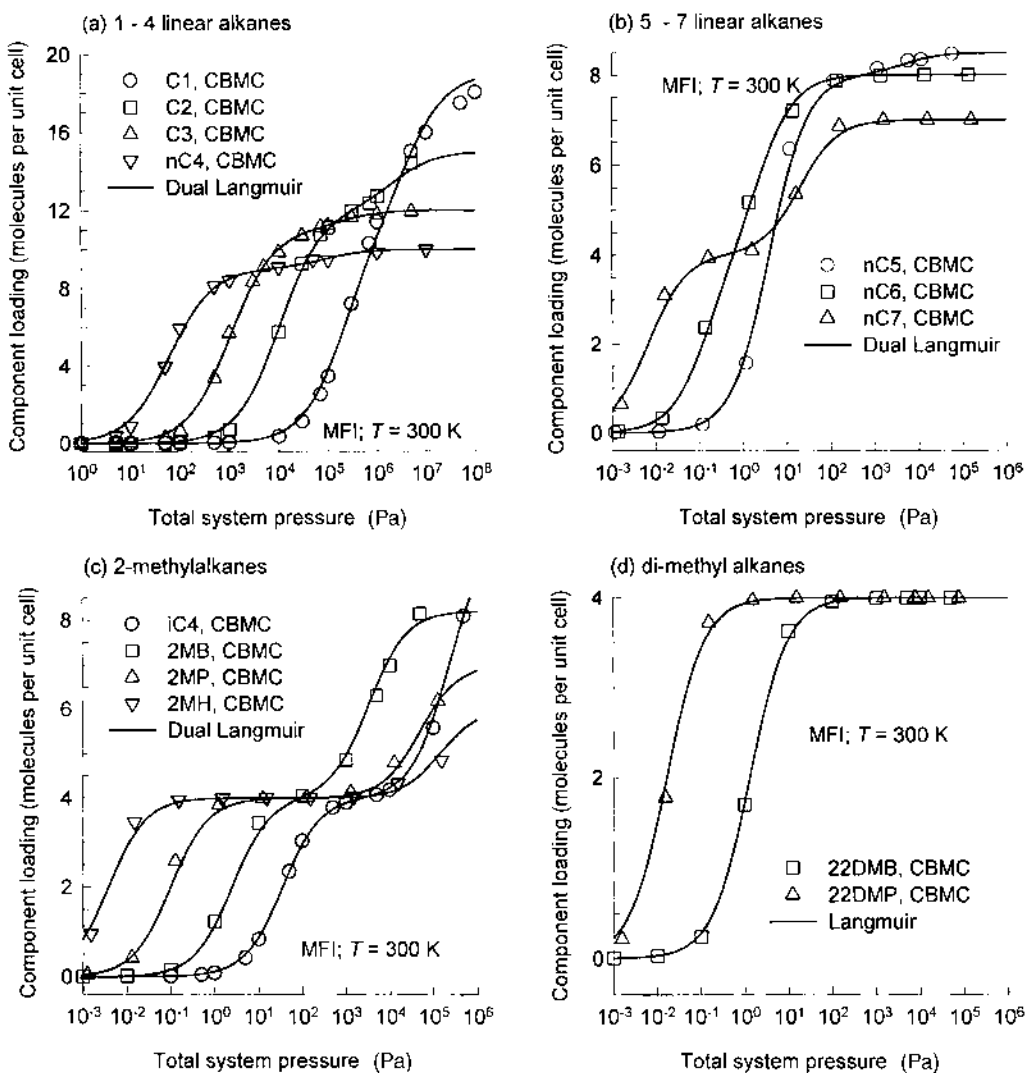
Fig. 5 Pure component isotherms for linear, 2-methyl- and dimethylalkanes in MFI at 300 K calculated using CBMC simulations (Refs. 14–21). The continuous lines represent the fits of the isotherms using the dual-site Langmuir model with parameters given in Table 1.

and the subscripts A and B refer to two sorption sites within the MFI structure, with different sorption capacities and sorption strengths. The $\Theta_{i,\text{sat,A}}$ and $\Theta_{i,\text{sat,B}}$ represent the saturation capacities of sites A and B, respectively. The fitted parameters for the pure component isotherms, shown in Fig. 5, are listed in Table 1. It is to be noted that the total saturation loading $\Theta_{i,\text{sat}} = \Theta_{i,\text{sat,A}} + \Theta_{i,\text{sat,B}}$ is not a fitted parameter but taken from the final plateau value of the sorption isotherm, estimated from CBMC simulations. In general, the saturation loading decreases with increasing carbon number and with increased degree of branching; see Fig. 6.

Table 1 Dual-Site Langmuir Parameters for Pure Alkanes in MFI at 300 K[a]

| | Dual Langmuir parameters | | | |
| | Site A | | Site B | |
Component	$b_{i,A}$ (Pa^{-1})	$\Theta_{i,\text{sat,A}}$ (molecules per unit cell)	$b_{i,B}$ (Pa^{-1})	$\Theta_{i,\text{sat,B}}$ (molecules per unit cell)
C1	4.86×10^{-6}	11.0	2.38×10^{-7}	8.0
C2	9.73×10^{-5}	12.0	4.38×10^{-7}	3.0
C3	9.64×10^{-4}	11.0	5.06×10^{-6}	1.0
nC4	1.63×10^{-2}	9.0	1.14×10^{-5}	1.0
nC5	0.25	8.0	2×10^{-4}	0.5
2MB	0.4	4.0	3×10^{-4}	4.2
nC6	7.0	4.0	0.4	4.0
2MP	10.0	4.0	2.0×10^{-5}	3.0
22DMB	0.76	4.0	—	0
nC7	150	4.0	5×10^{-2}	3.0
2MH	260	4.0	7×10^{-6}	2.0
22DMP	60	4.0	—	0

[a] Fits correspond to CBMC simulations.

The thermodynamic correction factor for the DSL model is

$$\Gamma = \frac{1}{\frac{\Theta_{i,A}}{\Theta_i}\left(1 - \frac{\Theta_{i,A}}{\Theta_{i,sat,A}}\right) + \frac{\Theta_{i,B}}{\Theta_i}\left(1 - \frac{\Theta_{i,B}}{\Theta_{i,sat,B}}\right)} \tag{17}$$

Calculations of the thermodynamic correction factor for linear and 2-methylalkanes are shown in Fig. 7. The thermodynamic correction factor for nC7 and all 2-methylalkanes
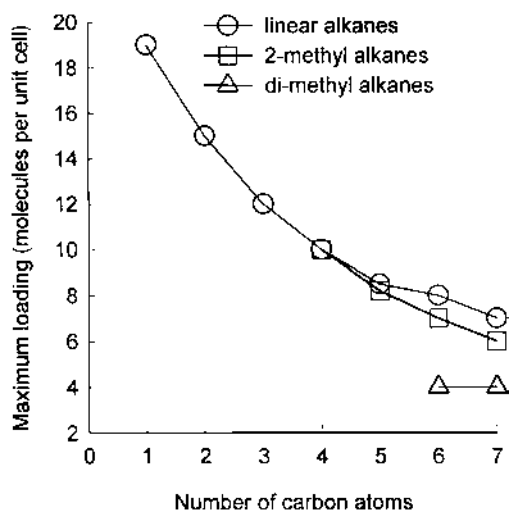

Fig. 6 Maximal saturation loadings of linear, 2-methyl- and dimethylalkanes in MFI at 300 K. CBMC calculations at 300 K using NVT simulations. (From Ref. 16.)
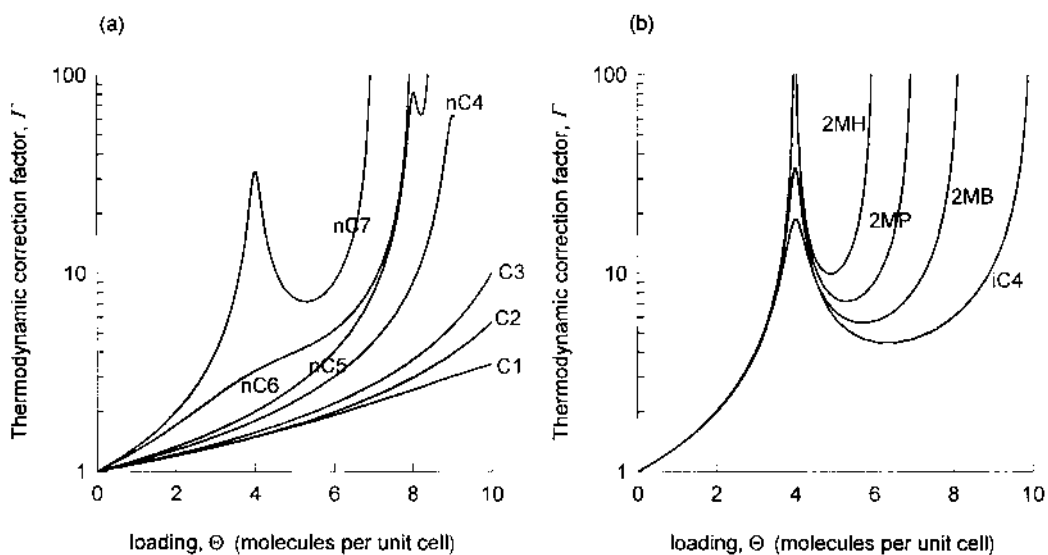
Fig. 7 Thermodynamic factor for (a) linear alkanes and (b) 2-methylalkanes in MFI at 300 K calculated using the dual-site Langmuir (DSL) model. DSL parameters given in Table 1.

shows two extrema: a maximum at the inflection point $\Theta = \Theta_{i,\text{sat,A}} = 4$ and a minimum at a loading $\Theta_{i,\text{sat,A}} < \Theta < \Theta_{i,\text{sat,A}} + \Theta_{i,\text{sat,B}}$.

The isotherm inflection for 2-methylalkanes is due to preferential location of molecules at the intersection. Inflection behavior is also exhibited by benzene in MFI at $T = 303$ K due to phase transitions (Fig. 8a). Since the Fick diffusivity is proportional to the thermodynamic factor, it can be expected to also exhibit two extrema if the Maxwell-Stefan diffusivity has a negligible loading dependence. This is verified by the experimental data of Shah et al. (9); see Fig. 8c.

In order to illustrate the influence of isotherm inflection on the uptake characteristics, let us consider desorption of 3-methylpentane (3MP) from MFI zeolite at a temperature of 362 K. The DSL isotherm parameters, obtained from CBMC simulations (14–21), are specified in Table 2. Initially the crystals are equilibrated by exposing to surrounding 3MP vapor at a pressure $p_{i,0} = 100$ kPa. The equilibrium loading within MFI is uniform and $\Theta_{i,0} = 5.596$ molecules per unit. At time $t = 0$, the surface of the zeolite crystals is exposed to 3MP vapor at a partial pressure $p_{i,s} = 0.5$ Pa, which gives an equilibrium loading at the outer surface $\Theta_{i,s} = 0.093$. Numerical solution of the partial differential equation (2), with the initial and boundary conditions given by Eqs. (11) and (12), yields the $\Theta_i(t)$ shown in Fig. 9a. We note an inflection in the desorption kinetics, indicated by the arrow. Figure 9b compares the desorption and adsorption kinetics of 3MP. The desorption kinetics are much slower than the adsorption kinetics; this is evidenced by the fact that at $Fo \equiv Dt/r_c^2 = 0.04$, the adsorption process is nearly at equilibrium whereas the desorption process has still a long way to go to equilibration.

A three-site model for sorption of aromatics on ZSM-5 has been proposed by Rudzinski et al. (23) to account for two inflection points observed under certain temperature conditions. The consequences for diffusion can be expected to be interesting but there is no experimental evidence in the literature.
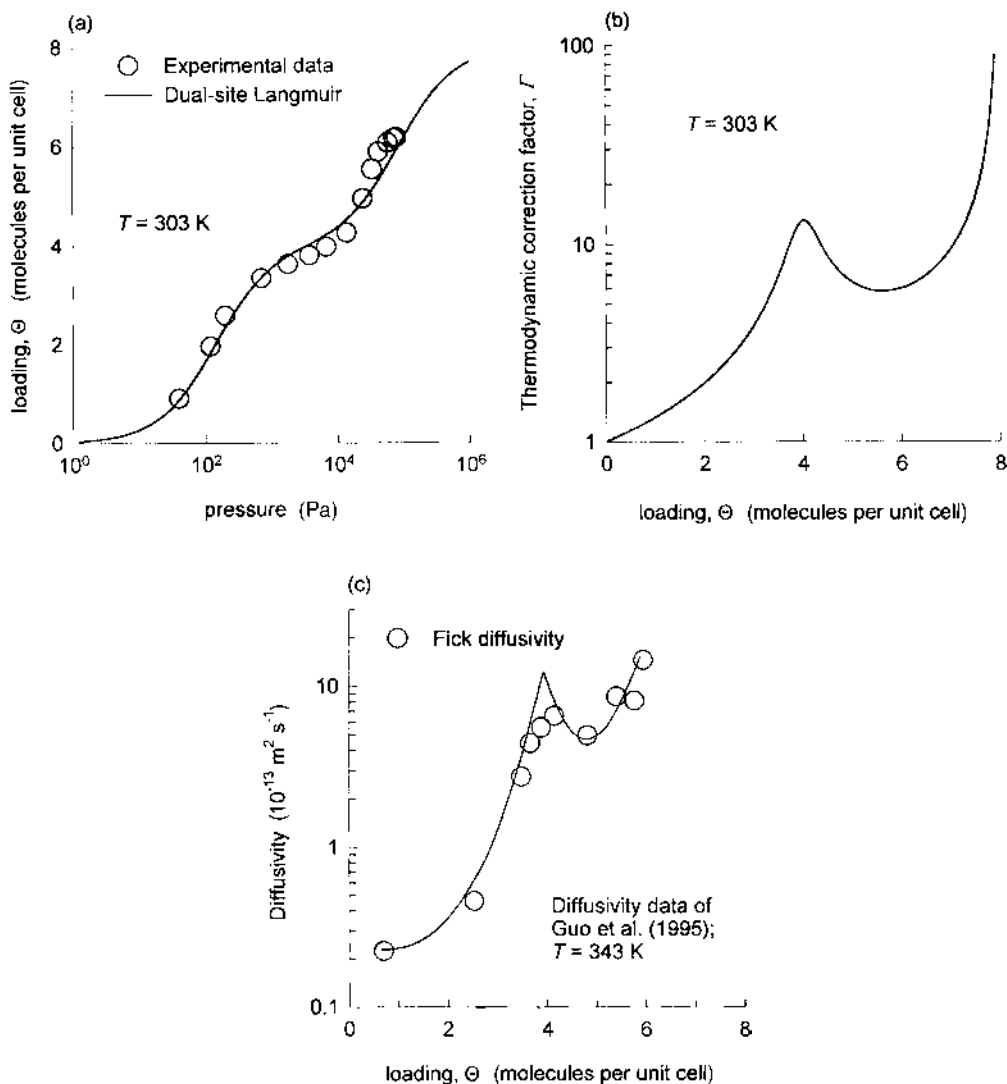
Fig. 8 (a) Pure component isotherms for sorption of benzene on MFI at a temperature of 303 K. (Experimental data from Ref. 8.) The dual-site Langmuir model parameters are $\Theta_{sat,A} = 4$, $\Theta_{sat,B} = 4$, $b_{1,A} = 7 \times 10^{-3}$ Pa^{-1}, $b_{1,B} = 1.2 \times 10^{-5}$ Pa^{-1}. (b) The thermodynamic correction factor calculated using the DSL model. (c) Fick diffusivity data for benzene in MFI at 303 K. (Data from Ref. 9.)

III. PERMEATION OF SINGLE COMPONENT ACROSS ZEOLITE MEMBRANE

Zeolite membranes are currently being developed for carrying out separations and catalytic reactions. It is important in practice to determine the permeation fluxes across the membrane. Most commonly, zeolite membrane devices are operated under steady-state conditions, though laboratory experiments also monitor the transience prior to achievement of steady state (24–26).

Table 2 Dual-site Langmuir Parameters for Hexane Isomers in MFI[a]

Component	Temp. (K)	Site A $b_{i,A}$ (Pa^{-1})	Site A $\Theta_{i,\text{sat},A}$ (molecules per unit cell)	Site B $b_{i,B}$ (Pa^{-1})	Site B $\Theta_{i,\text{sat},B}$ (molecules per unit cell)
nC_6	362	6.32×10^{-2}	4.0	1.7×10^{-3}	4.0
3MP	362	4.75×10^{-2}	4.0	2.27×10^{-5}	2.3

[a] Fits correspond to CBMC simulations (from Ref. 30).

We focus here on the permeation of a single component, species i, from a well-mixed upstream compartment, across the membrane, to a well-mixed downstream compartment. The permeate gases are often flushed out of the downstream compartment by means of a "sweep" gas (e.g., helium) in order to maintain the partial pressures of the permeants at low values; see Fig. 10. The zeolite crystals are deposited, or grown, onto a support layer consisting, say, of metal wool and/or a macroporous layer of sintered stainless steel particles (25,26). The diffusion through the support layer is akin to transport through the macropores within a sorbent particle and has been considered in detail by van de Graaf (25). The zeolite layer may have nanoscopic defects such as voids and pinholes that can be modeled in the manner described by Nelson et al. (27). In the following we ignore the support resistance and concentrate on the permeation characteristics of a defect-free zeolite membrane layer (of thickness δ). The upstream and downstream faces of the zeolite
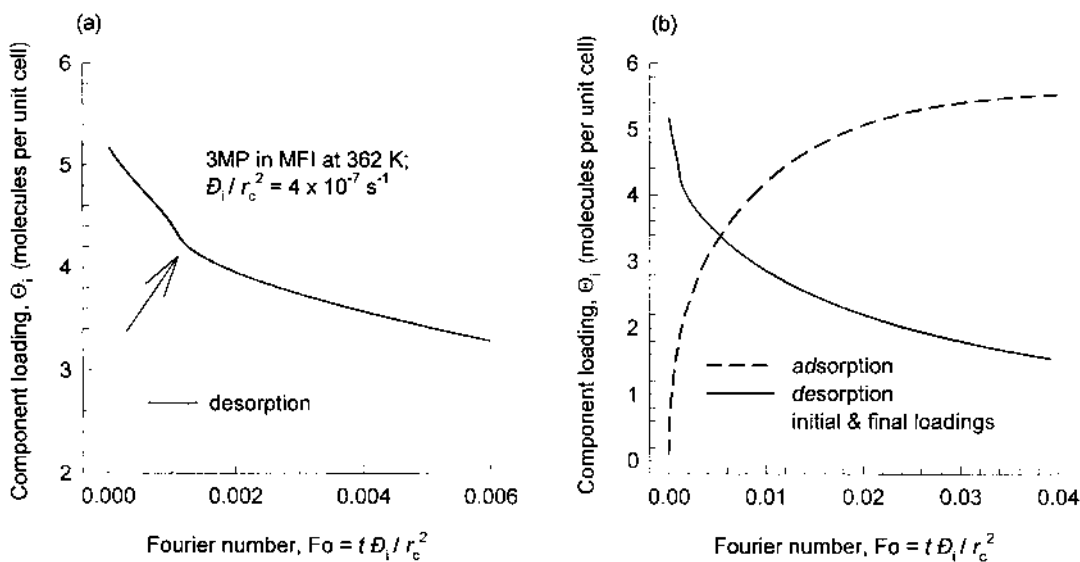

Fig. 9 (a) Kinetics of desorption of 3MP in MFI at 362 K. (b) Comparison of adsorption and desorption kinetics for 3MP.
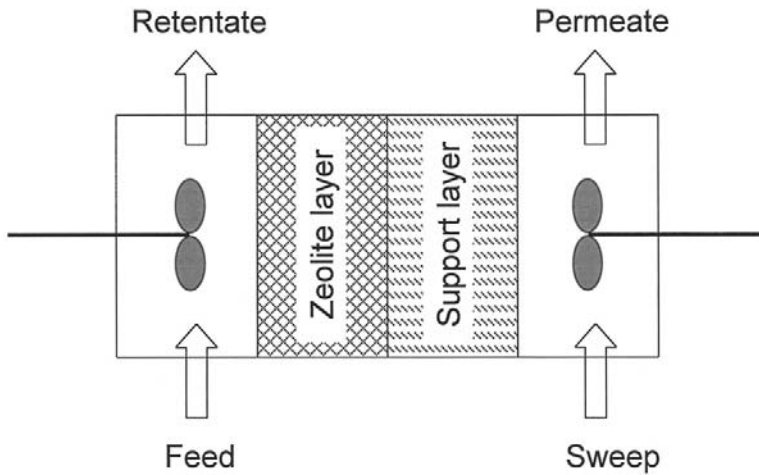
Fig. 10 Schematic of zeolite membrane separation device.

layer are assumed to be in equilibrium with the upstream and downstream partial pressures of the species, respectively:

Upstream face: $z = 0$; $\quad p_i = p_{i,0}$; $\quad q_i = q_{i,0}$; $\quad \Theta_i = \Theta_{i,0}$; $\quad \theta_i = \theta_{i,0}$ (18)

Downstream face: $z = \delta$; $\quad p_i = p_{i,\delta}$; $\quad q_i = q_{i,\delta}$; $\quad \Theta_i = \Theta_{i,\delta}$; $\quad \theta_i = \theta_{i,\delta}$ (19)

The permeation flux is obtained by solving

$$\frac{\partial \theta_i}{\partial t} = -\frac{1}{\rho \Theta_{i,sat}} \frac{\partial N_i}{\partial z}$$ (20)

where Eq. (3) is used to describe the single-component permeation flux.

A. Permeation of Methane and *n*-Butane Across MFI Membrane

For illustration, let us consider transient permeation of methane (C1) across a MFI membrane at 300 K. The upstream partial pressure of C1 is held at $p_{i,0} = 50$ kPa. The downstream pressure $p_{i,\delta}$ is maintained at vanishing values by means of a sweep gas. Taking the Maxwell-Stefan diffusivity of methane as $Đ_i = 10^{-9}$ m^2/s, along with the DSL isotherm parameters reported in Table 1, Eq. (20) can be solved to follow the transience in permeation flux N_i as steady state is approached; the results are shown in Fig. 11. At steady state, the permeation flux of methane is 19.46 mmol/m^2/s. For identical upstream and downstream partial pressures, the permeation of *n*-butane (*n*C4), with $Đ_i = 10^{-11}$ m^2/s, DSL parameters (also given in Table 1) show a much slower approach to the steady-state value of 4.65 mmol/m^2/s (see Fig. 11) because of its much lower diffusivity value.

For a 50:50 mixture of C1 (1) and *n*C4 (2), each with a 50-kPa upstream partial pressure, we might expect the permeation selectivity, S_P, defined by

$$S_p = \frac{N_2/N_1}{p_{20}/p_{10}}$$ (21)

to be 4.65/19.46 = 0.239. We will see later that this expectation is far removed from reality because of the peculiarities of mixture diffusion in zeolites.
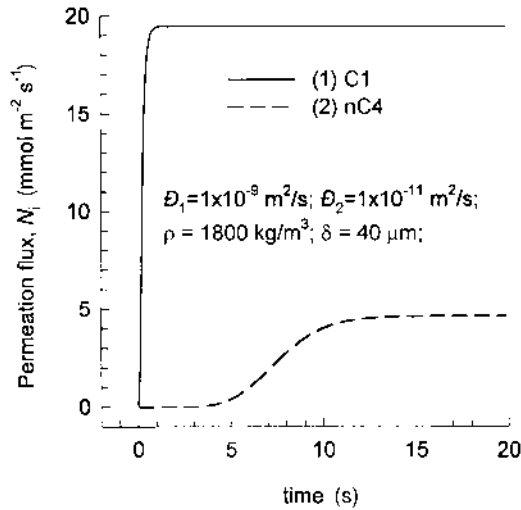
Fig. 11 Single-component transient permeation of methane (C1) and *n*-butane (*n*C4) across MFI membrane at 300 K.

IV. MODELING MIXTURE DIFFUSION WITH THE MAXWELL-STEFAN FORMULATION

For *n*-component diffusion the fluxes N_i are related to the gradients of the fractional occupancies by the generalization of Fick's law:

$$(\mathbf{N}) = -\rho[\Theta_{sat}][D]\frac{\partial(\theta)}{\partial r} \tag{22}$$

where $[D]$ is the *n*-dimensional square matrix of Fick diffusivities; $[\Theta_{sat}]$ is a diagonal matrix with elements $\Theta_{i,sat}$, representing the saturation loading of species *i*. The fractional occupancies θ_i are defined by Eq. (4). The estimation of the $n \times n$ elements of $[D]$ is complicated by the fact that these are influenced not only by the species mobilities (i.e., diffusivities $Đ_i$) but also by the sorption thermodynamics. In setting up a proper mixture diffusion theory we need to use chemical potential gradients as the proper driving forces. In the Onsager irreversible thermodynamics (IT) formulation, we generalize Eq. (5) in the following manner:

$$(N) = -\rho[\Theta_{sat}][L]\frac{1}{RT}\frac{\partial(\mu)}{\partial r} \tag{23}$$

where $\frac{\partial(\mu)}{\partial r}$ is the column matrix of chemical potential gradients; $[L]$ is the square matrix of Onsager coefficients having the units $[m^2\ s^{-1}]$. The Onsager matrix $[L]$ is nondiagonal, in general, and the cross-coefficients portray the coupling between species diffusion. The Onsager reciprocal relations demand that the matrix $[L]$ be symmetrical, i.e.,

$$L_{ij} = L_{ji}; \qquad i,j = 1,2,\ldots,n \quad (i \neq j) \tag{24}$$

The chemical potential gradients in Eq. (23) may be expressed in terms of the gradients of the occupancies by introduction of the matrix of thermodynamic factors $[\Gamma]$

$$\frac{\theta_i}{RT}\frac{\partial\mu_i}{\partial r} = \sum_{j=1}^{n}\Gamma_{ij}\frac{\partial\theta_j}{\partial r}; \quad \Gamma_{ij} \equiv \left(\frac{\Theta_{j,sat}}{\Theta_{i,sat}}\right)\frac{\Theta_i}{p_i}\frac{\partial p_i}{\partial\Theta_j}; \quad i,j = 1,2,\ldots,n \tag{25}$$

Knowledge of the sorption isotherm is sufficient to allow estimation of $[\Gamma]$ and $\frac{\partial(\mu)}{\partial r}$. If the n-component sorption can be described by the multicomponent Langmuir isotherm, the elements of $[\Gamma]$ are given by

$$\Gamma_{ij} = \delta_{ij} + \frac{\theta_i}{1-\theta_1-\theta_2-\ldots-\theta_n}; \quad i,j = 1,2,\ldots,n \tag{26}$$

where δ_{ij} is the Kronecker δ.

Combining Eqs. (23) and (25), we obtain

$$(N) = -\rho[\Theta_{sat}][L]\begin{bmatrix} 1/\theta_1 & 0 & 0 \\ 0 & \ddots & 0 \\ 0 & 0 & 1/\theta_n \end{bmatrix}[\Gamma]\frac{\partial(\theta)}{\partial r} \tag{27}$$

Comparing Eqs. (22) and (27), we obtain the interrelation:

$$[D] = [L]\begin{bmatrix} 1/\theta_1 & 0 & 0 \\ 0 & \ddots & 0 \\ 0 & 0 & 1/\theta_n \end{bmatrix}[\Gamma] \tag{28}$$

The Fick matrix $[D]$ can be estimated from knowledge of the Onsager matrix $[L]$. In general the thermodynamic correction factor matrix $[\Gamma]$ is nondiagonal and this makes multicomponent diffusion in zeolites a strongly coupled process.

Unfortunately, the IT theory provides no fundamental guidelines for estimating $[L]$ from data on pure component transport coefficients. For estimating $[D]$ it is more convenient to adopt the Maxwell-Stefan formulation, entirely consistent with the theory of IT, in which the chemical potential gradients are written as linear functions of the fluxes (28–31):

$$-\rho\frac{\theta_i}{RT}\nabla\mu_i = \sum_{\substack{j=1 \\ j\neq i}}^{n}\frac{\Theta_j\mathbf{N}_i - \Theta_i\mathbf{N}_j}{\Theta_{i,sat}\Theta_{j,sat}\mathcal{D}_{ij}} + \frac{\mathbf{N}_i}{\Theta_{i,sat}\mathcal{D}_i}; \quad i = 1,2,\ldots,n \tag{29}$$

We have to reckon in general with two types of Maxwell-Stefan diffusivities: $\mathcal{D}_i$ and $\mathcal{D}_{ij}$. The $\mathcal{D}_i$ are the diffusivities that reflect interactions between species i and the zeolite matrix; they are also referred to as jump or "corrected" diffusivities in the literature (1–4) and can be identified with the pure component transport parameters. There are two types of loading dependences which the $\mathcal{D}_i$ exhibit: (a) for weak confinement of guest molecules, $\mathcal{D}_i = \mathcal{D}_i(0)$, the zero-loading pure component diffusivity, and (b) for strong confinement $\mathcal{D}_i = \mathcal{D}_i(0)(1-\theta_i)$. In all of the illustrative examples to be presented below we assume the weak confinement scenario to hold.

Mixture diffusion introduces an additional complication due to guest$_i$–guest$_j$ interactions. This interaction is embodied in the "interchange" or "exchange" coefficients $\mathcal{D}_{ij}$. We can consider this coefficient as representing the facility for counterexchange, i.e., at a sorption site the guest species j is replaced by the species i. For intersecting channel structures such as MFI (see Fig. 12a) the interchange process takes place predominantly
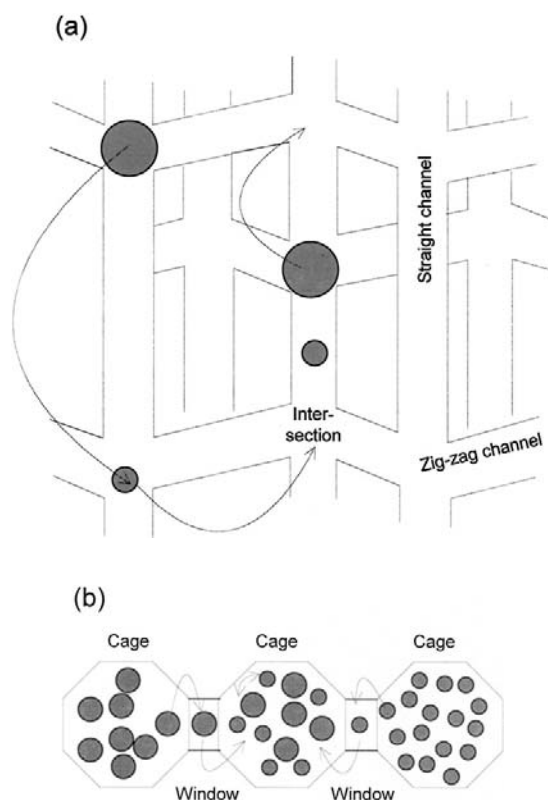
Fig. 12 Pictorial representation of the molecular jumps in (a) MFI structure and (b) cages separated by windows.

at the channel intersections. In structures such as LTA and FAU, molecule–molecule exchange takes place predominantly within the cages (Fig. 12b). The Onsager reciprocal relations require $Đ_{ij} = Đ_{ji}$. The net effect of this counterexchange is a slowing down of a faster moving species due to interactions with a species of lower mobility. Also, a species of lower mobility is accelerated by interactions with another species of higher mobility. An alternative interpretation is to regard $Đ_{ij}$ as quantifying vacancy correlation effects (32–34). For structures such as MFI, consisting of a three-dimensional network of intersecting straight and zig-zag channels, there is a strong correlation between the molecular jumps and the inclusion of the interchange coefficients $Đ_{ij}$ is essential in describing the mixture diffusion process; this has been verified by Paschek and Krishna (34) using kinetic Monte Carlo (KMC) simulations. For estimation of the $Đ_{ij}$ within MFI, they show that the logarithmic interpolation formula, suggested by Krishna and Wesselingh (28):

$$Đ_{ij} = [Đ_i]^{\theta_i/(\theta_i+\theta_j)}[Đ_j]^{\theta_j/(\theta_i+\theta_j)} \tag{30}$$

is of sufficient accuracy.

We now try to interrelate the MS formulation with the Onsager and Fick formulations; to do this we define an n-dimensional square matrix $[B]$ with elements

$$B_{ij} = \frac{1}{Đ_i} + \sum_{\substack{j=1 \\ j \neq i}}^{n} \frac{\theta_i}{Đ_{ij}}; \quad B_{ij} = \frac{\theta_j}{Đ_{ij}}; \quad i, j = 1, 2, \ldots, n \tag{31}$$

With this definition of $[B]$, Eq. (29) can be cast in n-dimensional matrix form:

$$(N) = -\rho[\Theta_{sat}][B]^{-1}[\Gamma]\frac{\partial(\theta)}{\partial r} \tag{32}$$

which gives the following expressions for the Onsager and Fick matrices

$$[L] = [B]^{-1} \begin{bmatrix} \theta_1 & 0 & 0 \\ 0 & \ddots & 0 \\ 0 & 0 & \theta_n \end{bmatrix}; \quad [D] = [B]^{-1}[\Gamma] \tag{33}$$

For single-component diffusion, Eq. (33) simplifies to Eq. (8). Equations (31) and (33) show that the interchange coefficients $Đ_{ij}$, portraying correlated molecular jumps, will influence *all* the elements of $[L]$ and $[D]$. Put another way, the main elements of the Onsager matrix L_{ii} cannot be identified with pure component diffusion coefficients, as has been erroneously suggested in the literature by Sundaram and Yang (35). In general, the Fick $[D]$ matrix has large nondiagonal elements and, consequently, the flux of any species i is strongly coupled to that of all other diffusing species j in the mixture.

For facile particle–particle exchange, i.e., $Đ_{ij} \rightarrow \infty$, vacancy correlation effects tend to get washed out. Facile counterexchange of particles could occur, for example, within the cages of FAU and LTA zeolites when intracage hopping rates are high. We see from Eqs. (31) and (33) that when $Đ_{ij} \rightarrow \infty$, both $[B]$ and $[L]$ matrices reduce to diagonal matrices and the flux relations (29) simplify to give:

$$\mathbf{N}_j = -\rho\Theta_{i,sat}\frac{L_{ij}}{RT}\nabla\mu_j \equiv -\rho\Theta_{i,sat}D_i\frac{\theta_i}{RT}\nabla\mu_j; \quad i = 1, 2, \ldots, n \tag{34}$$

The off-diagonal elements of the Onsager matrix are also a reflection of (vacancy) correlation effects and the assumption of vanishing off-diagonal elements of $[L]$ signifies vanishing correlation effects. The set of equations (34), with the multicomponent Langmuir model to estimate mixture isotherms [see Eq. (26)] were first developed by Habgood (36,37) to describe two-component diffusion in zeolite 4A. In zeolite 4A, the intracage hopping is not a limiting factor ($Đ_{ij} \rightarrow \infty$). The intercage hopping is governed by guest–host interactions only, as described by Eq. (34). The Habgood model is thus a special limiting case of the Maxwell-Stefan approach.

The mixture sorption characteristic influences mixture diffusion in two ways: (a) mixture sorption determines the magnitudes of the driving forces $\partial(\theta)/\partial r$, and (b) they contribute to *coupling* of the diffusion process due to the presence of the nondiagonal elements in $[\Gamma]$; even when Eq. (34) applies, the species diffusion is still coupled. The proper modeling of mixture sorption is the first essential step toward a proper modeling of mixture diffusion. In particular size and configurational entropy effects during mixture sorption need to be properly addressed. The entropy effects influencing mixture sorption also have a significant influence on mixture diffusion, as will be illustrated below by means of several illustrative examples (see also Chapter 9 in this volume).

V. ILLUSTRATIVE EXAMPLES OF BINARY MIXTURE DIFFUSION

A. Permeation of Methane–*n*-Butane Mixture Across MFI Membrane

Consider permeation of a 95:5 binary mixture of methane (C1) and *n*-butane (*n*C4) across an MFI membrane at 300 K. The first important step in modeling of diffusion is to model the pure component and mixture sorption characteristics; this is required in the determination of the component driving forces $\partial(\theta)/\partial r$ and the thermodynamic correction factors [Γ]. The pure component isotherms at 300 K in MFI zeolite, obtained from CBMC simulations, are shown in Fig. 5a, along with the DSL fits using the parameters specified in Table 1. For a 95:5 mixture of C1 and *n*C4, the component loadings in the mixture obtained from CBMC simulations are shown in Fig. 13a. The loading of C1 increases monotonically with increasing pressure. On the other hand the loading of *n*C4 reaches a plateau value for pressures in the 1- to 5-MPa range. Increasing the total system pressure beyond 5 MPa leads to a very slight decline in the loading of *n*C4. In Fig. 13b, we plot the sorption selectivity, S, defined by:

$$S = \frac{\Theta_2/\Theta_1}{p_2/p_1} \tag{35}$$

where p_1 and p_2 are the partial pressures in the bulk gas phase. For mixture loadings, $\Theta_{mix} = \Theta_1 + \Theta_2$, below 8, the sorption selectivity of *n*C4 with respect to C1 is practically constant and equals that calculated from the corresponding Henry coefficients, i.e., 2200. However, as Θ_{mix} increases beyond 8, the sorption selectivity decreases dramatically to values about one to two orders of magnitude lower. Near saturation loadings, the vacant spaces in the zeolite are more easily occupied by the smaller methane molecule. This is a size entropy effect that favors *smaller* molecules at high pressures. It is clear that size entropy effects counter the usual enthalpic effect of chain length; increase in the chain length favors the adsorption enthalpy of the *larger* molecule.
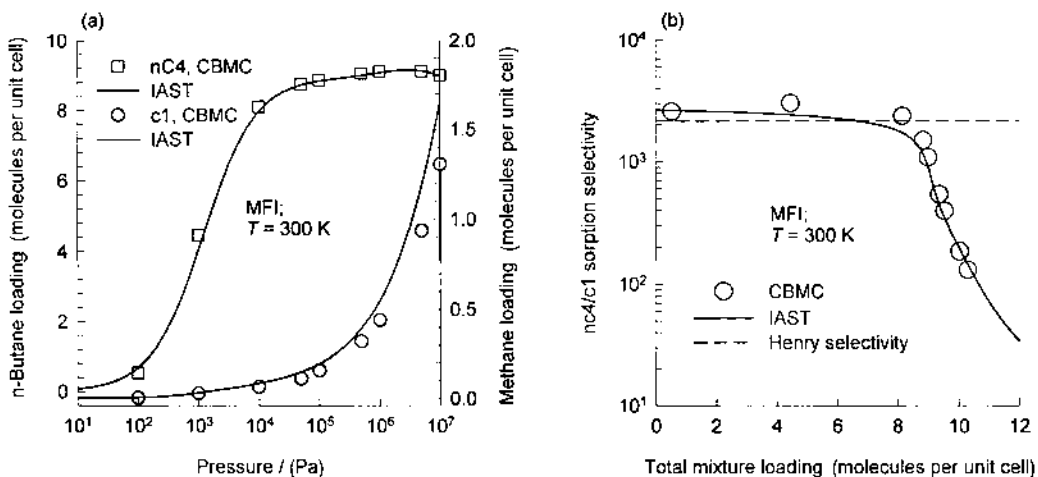

Fig. 13 (a) Sorption loadings of 95:5 binary mixture of C1 and *n*C4 in MFI at 300 K. (b) *n*C4/C1 sorption selectivity. The continuous lines represent the predictions of the IAST.

From a practical point of view, it is important to be able to predict the mixture isotherms from pure component isotherm data. It is clear that the multicomponent Langmuir isotherm will be totally unsuccessful in this regard because the sorption selectivity predicted by this model will be independent of the mixture loading. Let us try to estimate the mixture loadings from the pure component isotherms using the ideal adsorbed solution theory (IAST) of Myers and Prausnitz (38). Briefly, the basic equation of IAST theory is the analogue of Raoult's law for vapor–liquid equilibrium, i.e.:

$$Py_i = P_i^0(\pi)x_i; \quad i = 1, 2, \ldots, n \tag{36}$$

where x_i is the mole fraction in the adsorbed phase

$$x_i = \frac{\Theta_j}{\Theta_1 + \Theta_2 + \ldots \Theta_n} \tag{37}$$

and $P_i^0(\pi)$ is the pressure for sorption of every pure component i, which yields the same spreading pressure, π, as that for the mixture. The spreading pressure is defined by the Gibbs adsorption isotherm

$$\frac{\pi A}{k_B T} = \rho \int_{P=0}^{P=P_i^0} \frac{\Theta_i^0(P)}{P} dP \tag{38}$$

where A is the adsorben surface area per m^3 of adsorbent, k_B is Boltzmann's constant, ρ is the density of MFI expressed in terms of the number of unit cells per m^3, and $\Theta_i^0(P)$ is the pure component isotherm given by Eq. (16). The total amount adsorbed is obtained from

$$\Theta_{mix} \cong \Theta_1 + \Theta_2 \cdots + \Theta_n = \frac{1}{\frac{x_1}{\Theta_1^0(P_1^0)} + \frac{x_2}{\Theta_2^0(P_2^0)} + \cdots + \frac{x_n}{\Theta_n^0(P_n^0)}} \tag{39}$$

The set of Eqs. (16), (36)–(39) need to be solved numerically to obtain the loadings of the individual components in the mixture. We see in Fig. 13a and b that the IAST predictions are in excellent agreement with the CBMC simulation results. Size entropy effects are properly accounted for in the IAST mixture model.

Now let us consider permeation of the C1 (1) to nC4 (2) mixture across an MFI membrane for a situation with upstream partial pressures $p_{1,0} = 95$ kPa, $p_{2,0} = 5$ kPa. The downstream partial pressures $p_{i,\delta}$ are assumed to be maintained at vanishing values by means of a sweep gas. The boundary conditions, Eqs. (18) and (19), are thus determined. The set of differential equations (20) are solved together with the (coupled) flux Maxwell-Stefan relations (32) in order to obtain the fluxes N_i across the membrane. The results are shown in Fig. 14a. The steady-state fluxes of C1 and nC4 are found, respectively, to be 0.125 and 3 mmol/m^2/s giving an nC4/C1 permeation selectivity value [see Eq. (21)], $S_P = 456$. During the initial transience, the methane flux attains a maximum in the flux (with a value of 0.4 mmol/m^2/s) at $t = 1$ s. The reason for this peak is that during the initial period, methane that has a diffusivity value 100 times that of nC4 diffuses faster through the membrane. However, as time progresses the MFI structure gets increasingly occupied with nC4 that dislodges the less strongly adsorbed C1. The flux of nC4 is enhanced with increased nC4 loading. Concomitantly, the flux of C1 decreases because its loading in MFI decreases. Furthermore, in the Maxwell-Stefan model the interchange coefficient D_{ij} serves to slow down methane and speed up nC4. All these factors leads to a decline in the flux of C1 from its peak value of 0.4 to the steady-state value of 0.125 mmol/m^2/s.
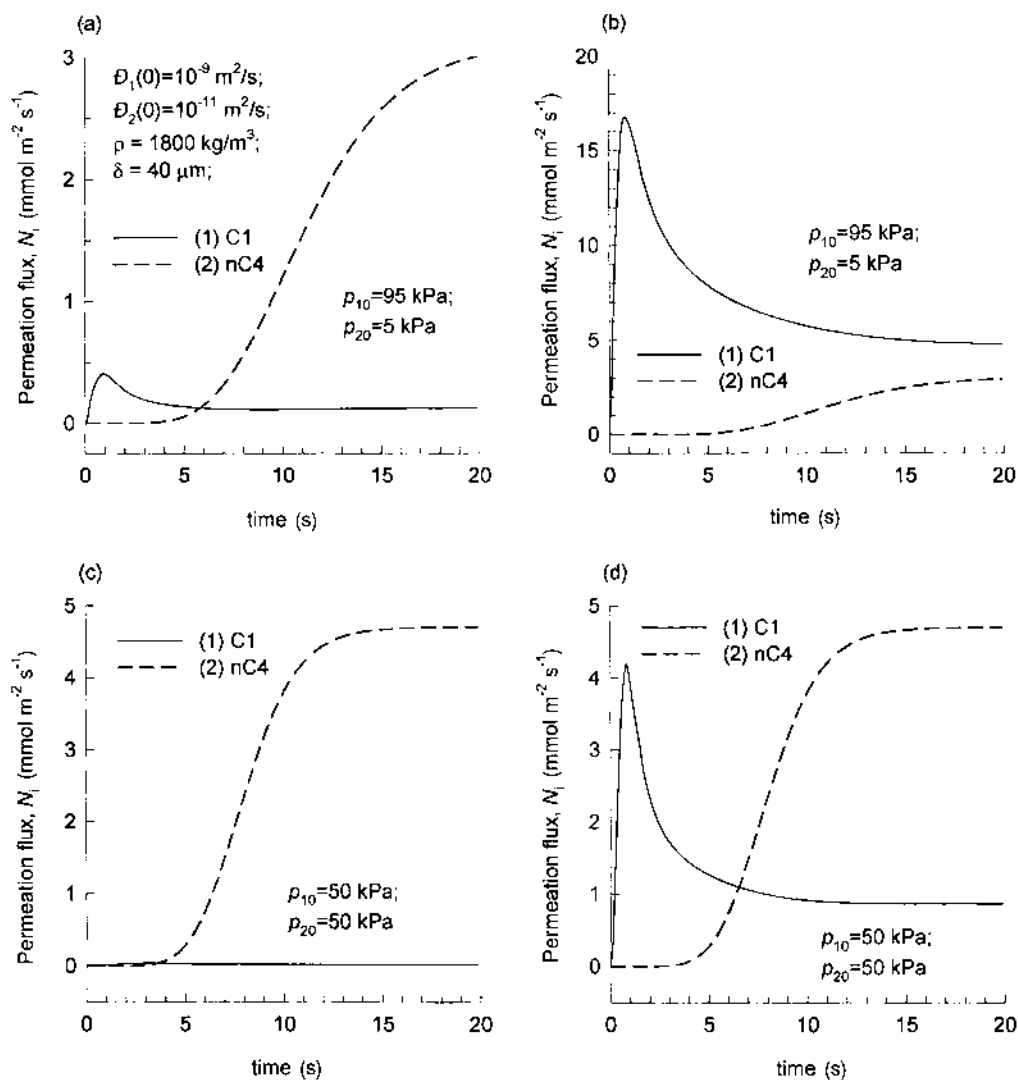
Fig. 14 (a, b) Transient permeation across MFI membrane of 95:5 mixture of C1 and nC4 in MFI at 300 K. (c, d) Transient permeation of 50:50 mixture of C1 and nC4 in MFI at 300 K. Two implementations of the Maxwell-Stefan model are compared, with finite and infinite interchange coefficients $Ð_{ij}$.

The predictions of the fluxes with the M-S model assuming $Ð_{ij} \rightarrow \infty$ and using Eq. (34) are shown in Fig. 14b. There is no slowing down of methane due to interchange and therefore the initial transience shows a peak methane flux of 17 mmol/m^2/s, which reduces at steady state to 4.8. Assuming $Ð_{ij} \rightarrow \infty$ has a less dramatic influence on the nC4 flux, which reaches a steady-state value of 2.96 mmol/m^2/s. The permeation selectivity is calculated as $S_P = 0.235$, significantly lower than the value of 456 using the complete Maxwell-Stefan theory with finite interchange. The experimental value of S_P for this 95:5 mixture determined by Bakker (26) is 380, quite close to the estimations of the Maxwell-Stefan model including interchange.
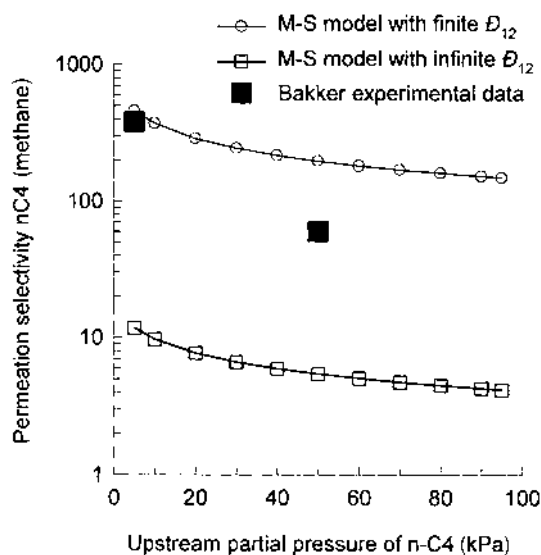
Fig. 15 Dependence of $nC4/C1$ permeation selectivity on the two implementations of Maxwell-Stefan model, with and without inclusion of the interchange coefficient $Đ_{ij}$. Also shown are the experimental data of Bakker (Ref. 26).

A similar picture emerges for permeation of a 50:50 mixture; see Fig. 14c and d. The respective values of the permeation selectivities are $S_P = 197$ and 5.4. The experimental value of S_P for this 50:50 mixture determined by Bakker (26) is 60. Clearly, the interchange process within MFI matrix occurs at a finite rate. In Sec. III.A we have calculated the permeation selectivity on the basis of pure component permeation to be 0.239. Clearly, these mixture permeation selectivities cannot be predicted on the basis of pure component permeation data.

We carried out a series of simulations with varying mixture compositions in the upstream membrane compartment, keeping the total upstream pressure at 100 kPa; the calculations of S_P with the Maxwell-Stefan model, both with finite interchange, following Eq. (30), and taking $Đ_{ij} \to \infty$, are shown in Fig. 15, along with the Bakker experimental data (26). The decrease in the permeation selectivity with increasing partial pressure of nC4 is essentially a size entropy effect that comes into play at high occupancies and favors the smaller methane molecule. If we had used the multicomponent Langmuir isotherm, taking the saturation capacities of C1 and nC4 to be equal to one another, the S_P would be predicted to be independent of the upstream composition and have a constant value of 800. Kapteijn et al. (29) and Krishna and Paschek (30) have analyzed permeation data for C1-C2 and C1-C3 mixtures across an MFI membrane to stress the need for recognizing the size entropy effects (with the use of the IAST model). Furthermore, the results in Fig. 15 underline the importance of the interchange coefficient $Đ_{ij}$ in the Maxwell-Stefan formulation described by Eq. (29).

B. Diffusion of nC_6−3MP Mixture in MFI Zeolite

Before analyzing diffusion we need to understand the pure component and mixture sorption behaviors. The pure component isotherms of hexane isomers nC_6 and 3MP in

MFI zeolite at 362 K, obtained from CBMC simulations, are shown in Fig. 16a. The loadings in a 50:50 mixture are shown in Fig. 16b. For $\Theta_{mix} < 4$ the isomers have practically the same sorption strength. However, the loading of the monobranched isomer reduces to very low values when $\Theta_{mix} > 4$. The reason for this "exclusion" of the 3MP is because of *configurational* entropy effects which tends to favor the linear isomer. For $\Theta_{mix} < 4$, the 3MP molecules prefer to locate at the intersections between the straight
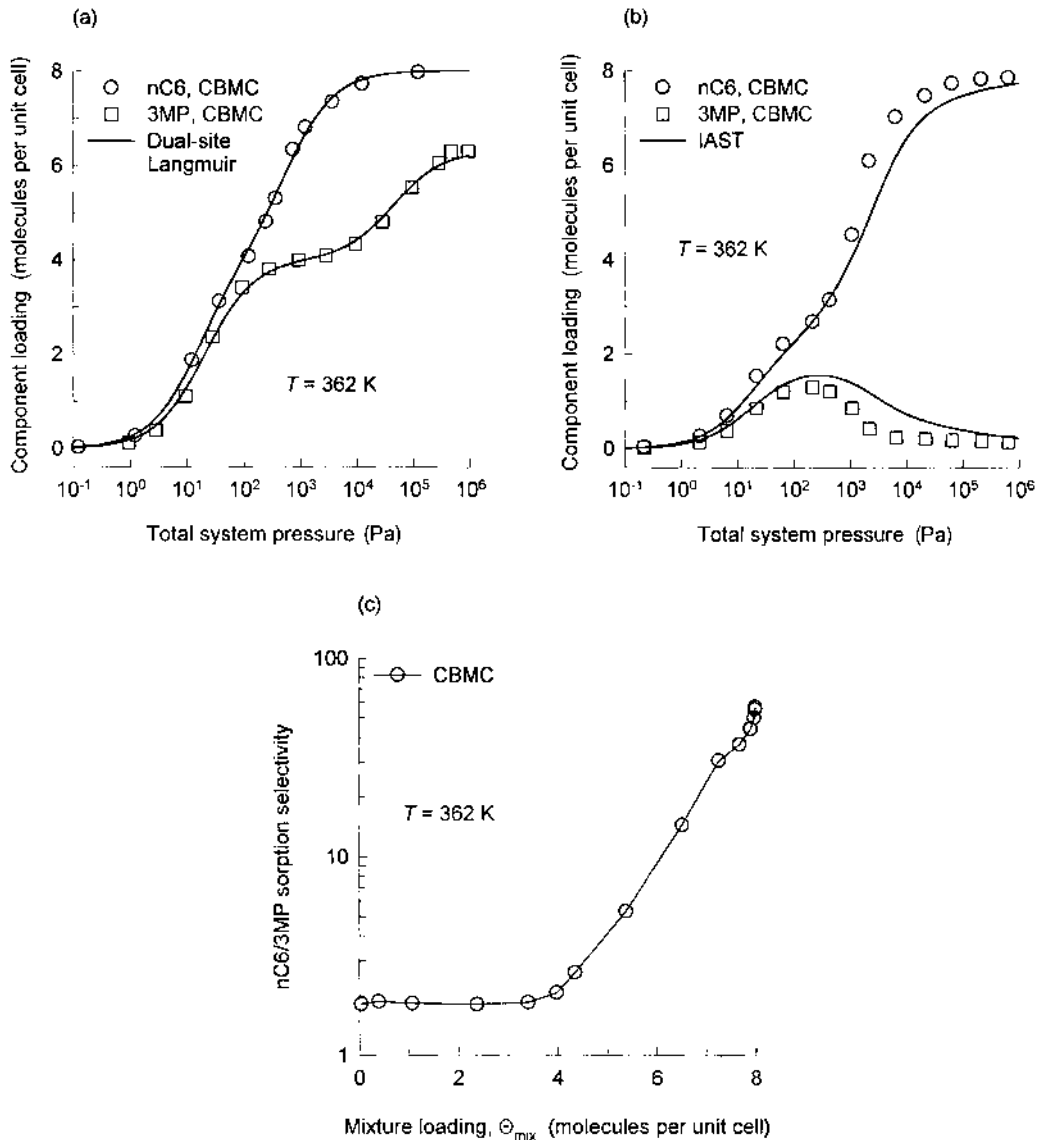

Fig. 16 (a) Pure component isotherms for nC_6 and 3MP in MFI at 362 K. CBMC calculations and DSL fits. (b) Component loadings for 50:50 mixture obtained from CBMC simulations compared with IAST predictions. (c) nC_6/3MP sorption selectivity as a function of the total mixture loading Θ_{mix}.

channels and zig-zag channels (16,17,30). The normal alkane can be located anywhere within the MFI matrix. At $\Theta_{mix} = 4$, all of the intersection sites are fully occupied. The 3MP demands an extra "push" to locate within the channel interiors (witness the inflection in the pure component isotherms in Fig. 16a. 3MP suffers a penalty from configurational entropy considerations because these molecules "pack" less efficiently within the MFI matrix; this penalty causes 3MP to be virtually excluded from the MFI matrix near saturation loadings $\Theta_{mix} = 8$. The sorption selectivity, S, defined by Eq. (35), is plotted in Fig. 16c as a function of the total mixture loading; S increases significantly above unity values when the mixture loading Θ_{mix} exceeds four molecules per unit cell.

Also shown in Fig. 16b are the IAST calculations of the component loadings with the DSL parameters reported in Table 2. These are in reasonably good agreement with the CBMC simulation results; it appears that the IAST mixture rule properly accounts for configurational entropy effects. Clearly, such effects are not accounted for by the multi-component Langmuir model to predict mixture behavior.

Let us now consider the uptake of pure components nC_6 (1) and 3MP (2) into a (virgin) spherical MFI crystallite at 362 K. At time $t = 0$, the outer surface of the crystal is exposed to a vapor phase with $p_{1,s} = 50$ kPa; $p_{2,s} = 50$ kPa; these partial pressures are maintained until equilibrium is achieved. The pure component uptake kinetics, obtained by solution of Eqs. (2), (3), together with (16), are shown in Fig. 17a. In these calculations the pure component Maxwell-Stefan diffusivities are taken to be equal $Đ_i/r_c^2 = 4 \times 10^{-7}$ s^{-1} for either isomer. The uptake of a 50:50 mixture of nC_6 (1) and 3MP (2) with $p_{1,s} = 50$ kPa; $p_{2,s} = 50$ kPa, calculated with the Maxwell-Stefan equations (29)–(32) are shown in Fig. 17b. The maximum in the transient loading of 3MP is noteworthy; this maximum is a direct consequence of the maximum in the mixture sorption seen in Fig. 16b. We also note that at equilibrium, the branched isomer is virtually excluded from the MFI matrix. The calculations for the uptake using the Maxwell-Stefan model with $Đ_{ij} \rightarrow \infty$, Eq. (34), are shown in Fig. 17c. The results are only slightly different from the Maxwell-Stefan model including $Đ_{ij}$. This result is to be expected because we had assumed the pure component Maxwell-Stefan diffusivities to be equal for either isomer; there is essentially no speeding up or slowing down of either molecule due to mobility differences. The small differences between the complete Maxwell-Stefan model, Eq. (29) and the simplified Eq. (34) are to be ascribed to the differences in the sorption loadings of nC_6 and 3MP and the influences of these component loadings on the diffusion behavior via the [Γ] matrix.

The mixture results shown in Fig. 17 are of practical importance because they provide a means of separating the hexane isomers, relying on configurational entropy effects. The separation can be achieved by allowing equilibrium to be attained in a batch adsorber. We need to operate with ambient conditions such that mixture loading $\Theta_{mix} > 4$; at 362 K this corresponds to a total system pressure in excess of 10 kPa. There is some evidence in the patent literature that the entropy concept is being used in commercial practice to separate mixtures of linear and branched alkanes (39).

High selectivities for separation of the hexane isomers can also be achieved in a membrane permeation device. Consider permeation of an equimolar mixture of nC_6 and 3MP across an MFI zeolite membrane, keeping the upstream compartments at a total pressure of 2 kPa. The (normalized) transient permeation fluxes, calculated using the Maxwell-Stefan model are shown in Fig. 18a. The steady-state permeation selectivity S_P can be calculated to be 2.5. Simulations were carried out for a range of system pressures in the upstream compartment; the results for the fluxes and selectivity are shown in Fig. 18b and c, respectively. We note that values of S_P in excess of 10 can be obtained when the pressure in the upstream compartment increases beyond 20 kPa; the results in Fig. 18c
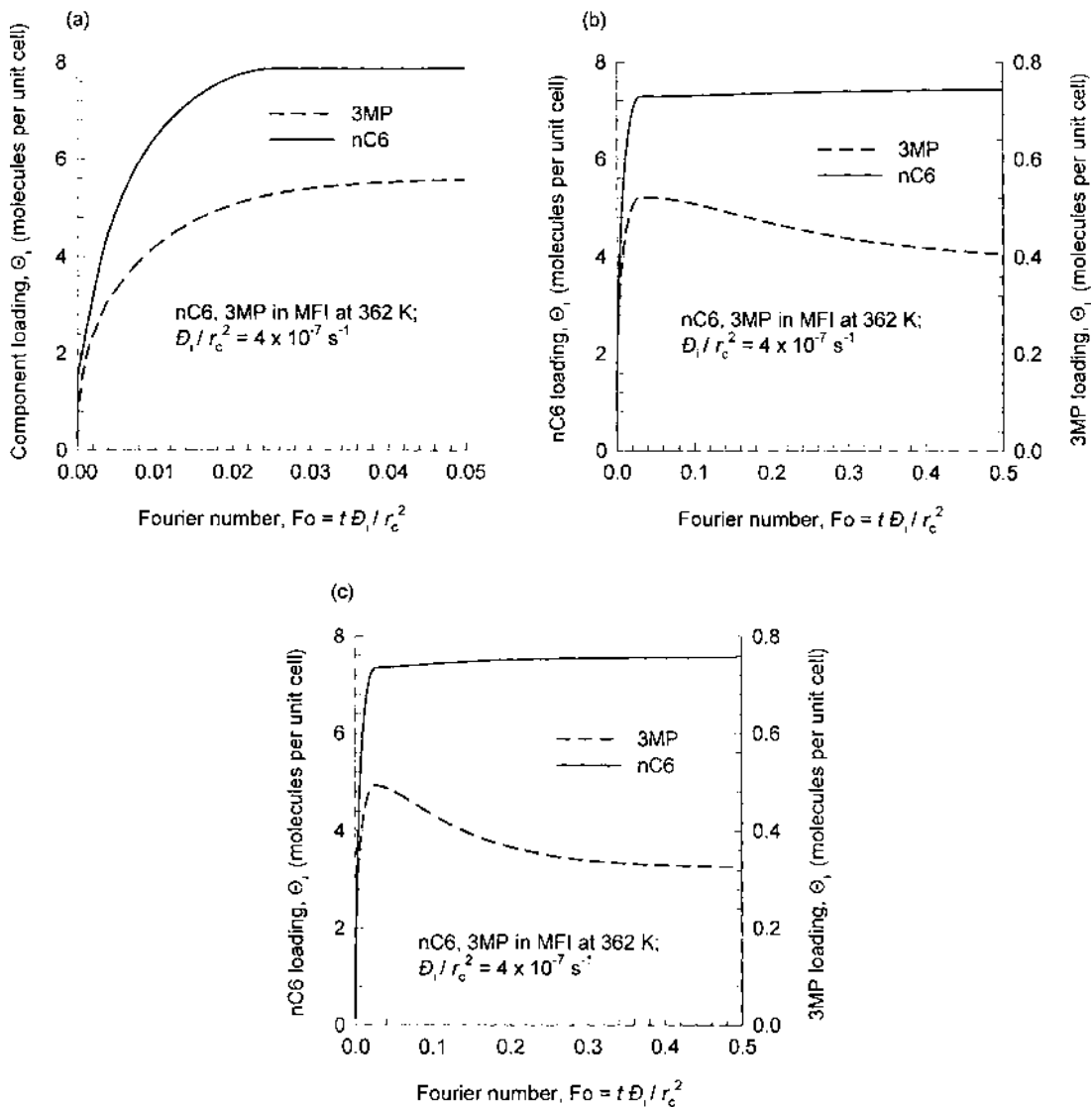
Fig. 17 (a) Transient uptake of pure components nC_6 and 3MP within spherical crystallite of MFI at 362 K. The bulk vapor phase partial pressures are 50 kPa for either component. (b) Transient uptake of 50:50 mixture of nC_6 and 3MP within spherical crystallite of MFI at 362 K. The bulk vapor phase partial pressures are 50 kPa for either component. The calculations are with the Maxwell-Stefan model with finite interchange coefficient $Đ_{ij}$. (c) Uptake of 50:50 mixture calculated with the Maxwell-Stefan model with $Đ_{ij} \to \infty$. The model parameters are given in Table 2.

mirror the sorption selectivity results shown in Fig. 16c. For operation with an upstream pressure of 15 kPa, Funke et al. (40) have experimentally determined a value S_P of 24; this is in reasonable agreement with our simulation results shown in Fig. 18c when we consider that our simulations were entirely based on CBMC simulations and no experimental data inputs were used. One reason for the higher S_P found experimentally is probably our assumption that the Maxwell-Stefan diffusivities are equal for either isomer. We would expect nC_6 to have a higher mobility than 3MP. More important is the
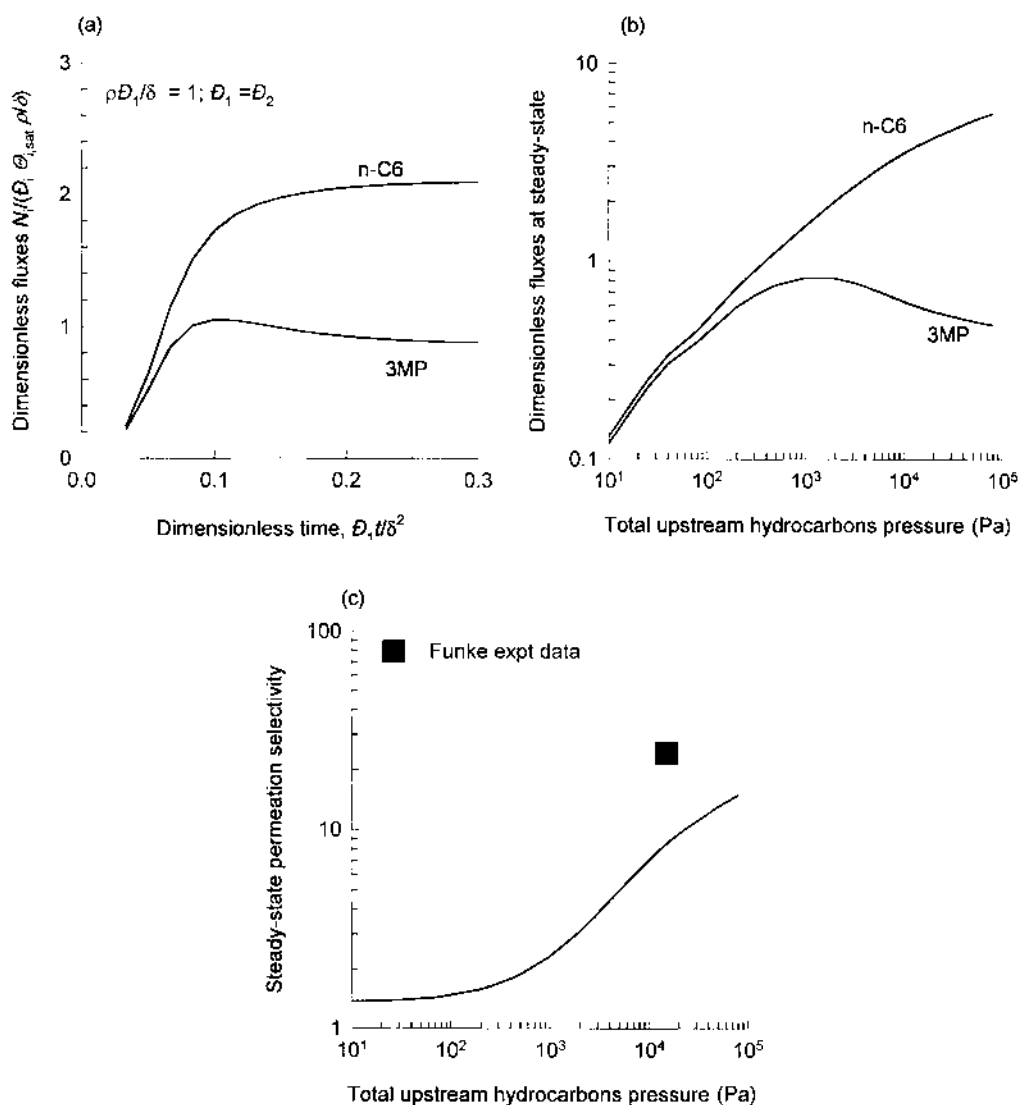
Fig. 18 (a) Transient diffusion fluxes for permeation of 50:50 mixture of nC_6 and 3MP across MFI membrane at 362 K. The upstream partial pressures are $p_{10} = 1$ kPa, $p_{20} = 1$ kPa. (b) Steady-state permeation fluxes as a function of upstream hydrocarbons pressure. The Maxwell-Stefan diffusivities of the isomers are taken to be equal, i.e. $Ð_1 = Ð_2$. (c) Separation selectivities as function of upstream hydrocarbons pressure. (The experimental data point in (c) is from Ref. 40.) The model parameters are given in Table 2. The Maxwell-Stefan model takes account of finite interchange coefficient $Ð_{ij}$, using Eq. (30).

observation of Funke et al. (40) that the permeation selectivity based on pure components was found to be only 1.3. This underlines the fact that subtle configurational entropy effects are at play here.

The same entropy principle can be used to separate nC_6 and 2,2-dimethylbutane (22DMB), as has been demonstrated by Gump et al. (41), and underpinned using CBMC simulations (42).

Table 3 Pure Component Langmuir Parameters and M-S Diffusivities for N_2 and CH_4 in 4A Zeolite at 193.7 K

Factor	N_2	CH_4
Saturation loading q_{sat} (mol kg^{-1})	3.75	3.86
Langmuir parameter, b (Pa^{-1})	1.08×10^{-4}	2.56×10^{-4}
$Đ_i$ (m^2 s^{-1})	3.9×10^{-18}	1.8×10^{-19}
Crystallite radius, r_c (m)	0.5×10^{-6}	

Source: Data from Ref. 36.

C. Diffusion of N_2 and CH_4 in Zeolite 4A

Consider uptake of N_2 and CH_4 into a spherical zeolite 4A crystal at 193.7 K. Experimental data for pure component sorption parameters and diffusivities have been published in the classic paper by Habgood (36); these data have been reported in Table 3. The pure component characteristics are interesting because while CH_4 has a higher sorption strength (witness the higher Langmuir b parameter in Table 3), its diffusivity is considerably lower. The uptake characteristics into 4A zeolite from a bulk vapor mixture maintaining $p_{N2} = 50.9$ kPa and $p_{CH4} = 49.1$ kPa are shown in Fig. 19. The Habgood data (open symbols) show that N_2 exhibits a peak during its transience to equilibrium. The reason for this is clear; starting with (virgin) zeolite, the initial loadings are dominated by the faster diffusing N_2. As time progresses, the slower diffusing but more strongly adsorbing CH_4 displaces N_2.

Using the pure component data in Table 3, simulations for the uptake were carried out with the Maxwell-Stefan model, both with finite interchange coefficient $Đ_{ij}$ calculated

Fig. 19 Transient uptake of 50.9% N_2, 49.1% CH_4 mixture into spherical crystallite of 4A zeolite at 193.7 K. (Experimental data from Ref. 36.) Two implementations of the Maxwell-Stefan model are compared, with finite and infinite interchange coefficient $Đ_{ij}$. The model parameters are given in Table 3.
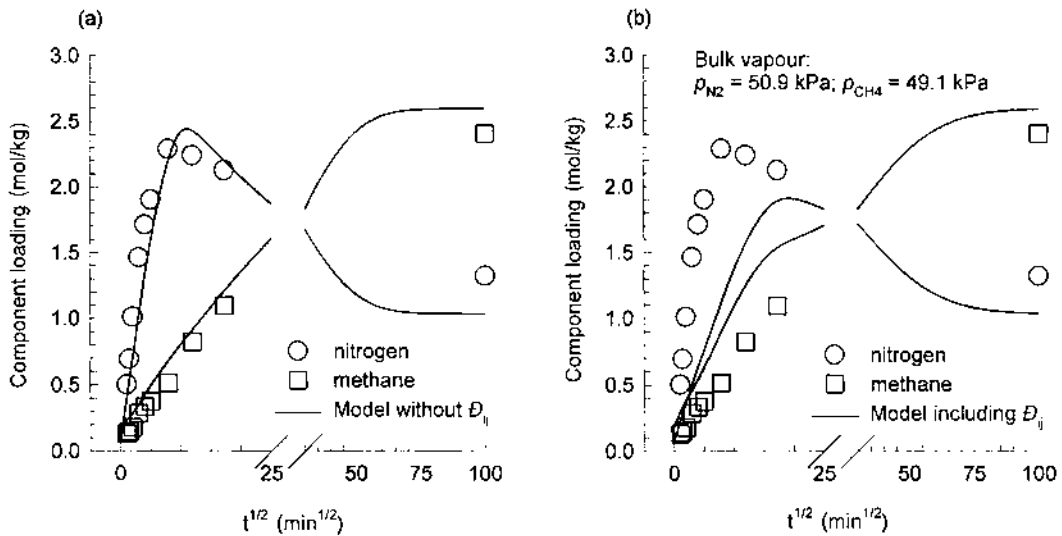
Fig. 20 Transient uptake of 10% N_2, 90% CH_4 mixture into spherical crystallite of 4A zeolite at 193.7 K. (Experimental data from Ref. 36.) Two implementations of the Maxwell-Stefan model are compared, with finite and infinite interchange coefficient $Ð_{ij}$. The model parameters are given in Table 3.

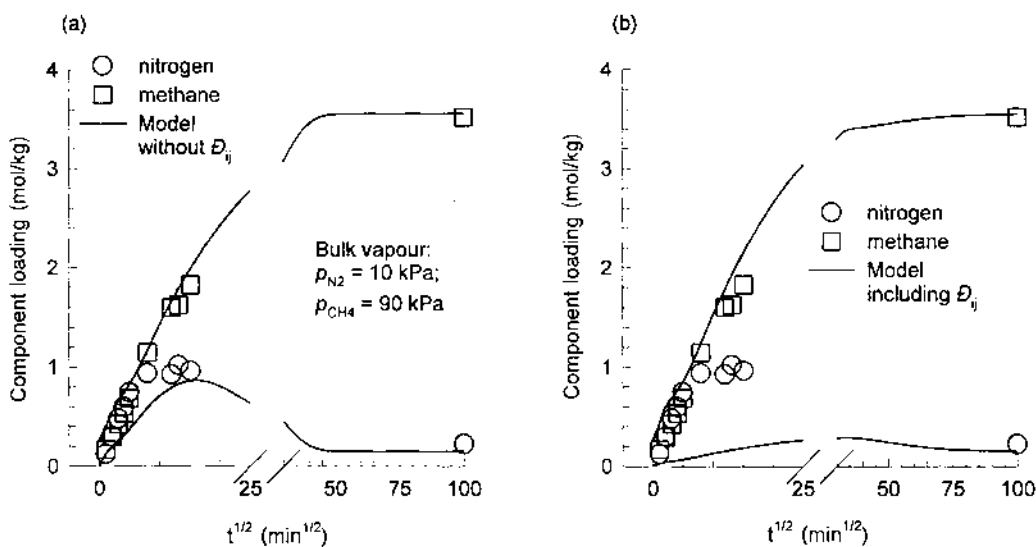using Eq. (30) (Fig. 19b) and taking $Ð_{ij} \to \infty$ (Fig. 19a). Both Maxwell-Stefan approaches predict a peak in the N_2 flux, but the model assuming $Ð_{ij} \to \infty$ does a much better job of quantitatively predicting the uptake profiles, which casts some doubt on the interpolation formula in Eq. (30). Habgood has also published experimental data for uptake into 4A zeolite from a bulk vapour mixture maintaining $p_{N2} = 10$ kPa and $p_{CH4} = 90$ kPa; these data are shown in Fig. 20, along with the two implementations of the Maxwell-Stefan model. Again we note that that Maxwell-Stefan model, assuming $Ð_{ij} \to \infty$ does a very good job of predicting the mixture diffusion behavior. It appears that diffusion of N_2 and CH_4 in the zeolite 4A sample used by Habgood proceeds following Eq. (34) and is essentially free from vacancy correlation effects.

D. Co- vs. Counterdiffusion of N_2 and CH_4

In the transient uptake shown in Fig. 19 we had codiffusion of N_2 and CH_4 within 4A zeolite. Let us focus on the transient uptake of N_2 and compare two situations: (a) with codiffusion of CH_4 and (b) with CH_4 diffusing in a direction countercurrent to N_2. The countercurrent scenario is achieved by preequilibrating the zeolite with CH4 exposing it to a bulk vapor with $p_{CH4} = 49.1$ kPa. This preequilibrated zeolite is then exposed to a bulk vapour with $p_{N2} = 50.9$ kPa. Simulations using the Maxwell-Stefan model, taking $Ð_{ij} \to \infty$, are compared in Fig. 21. The two uptake characteristics are markedly different. During codiffusion, N_2 and CH_4 compete for sorption sites because they move in the same "direction"; N_2 wins in the early stages, yields the majority of the sorption sites to CH_4 eventually. There is no competition during counterdiffusion but there is cooperation, CH_4 diffuses out and makes way for the incoming N_2.

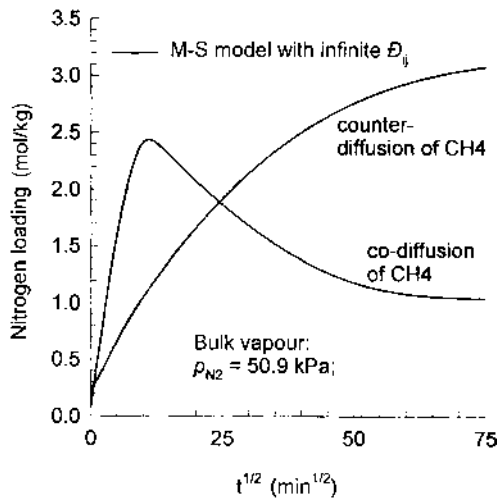The asymmetry in co- and counterdiffusion has also been verified in experimental studies (43).

Fig. 21 Comparison of transient uptake of N_2 with co- and counterdiffusion of CH_4 mixture into spherical crystallite of 4A zeolite at 193.7 K. The Maxwell-Stefan model calculations assumes $Đ_{ij} \to \infty$. The model parameters are given in Table 3.

E. Separation of O_2 and N_2 Using 4A Zeolite

The separation of O_2 from N_2, can be achieved by exploiting the differences in their diffusivities in small pore 4A zeolite. The separation process is commonly carried out in a packed bed of sorbent particles (Fig. 22). We now develop a model for breakthrough in this packed bed for the case in which intracrystalline diffusion is the controlling resistance. Assuming plug flow, the concentration at any position and instant of time obtained by solving the following set of partial differential equations (details can be found in Refs. 1–6,44–46).

$$\frac{\partial c_i}{\partial t} = -\frac{\partial (u c_i)}{\partial z} - \left(\frac{1-\varepsilon}{\varepsilon}\right)\rho\frac{\partial q_t}{\partial t} \tag{40}$$

where c_i is the molar concentration in the gas phase, u is the fluid phase (absolute) velocity, z is the axial coordinate distance, ε is the bed porosity, ρ is the density of the zeolite crystals, and q_i is the average concentration within the spherical particle given by Eq. (13). Usually the LDF approximation is made in order to avoid solving the intraparticle diffusion numerically. Furthermore, published models for breakthrough in packed beds (3,45,46) almost invariably use the multicomponent Langmuir isotherm to describe mixture diffusion. Use of either LDF or the multicomponent Langmuir isotherm is not to be recommended in the general case where subtle entropy effects come into play, affecting sorption and diffusion. For accurate modeling, therefore, there is no avoiding use of the IAST and using a rigorous solution of intracrystalline diffusion.

  Consider the breakthrough behavior for air (21% O_2, 79% N_2) at a pressure of 300 kPa in a packed bed of 0.6 m length; other details and parameters are specified in
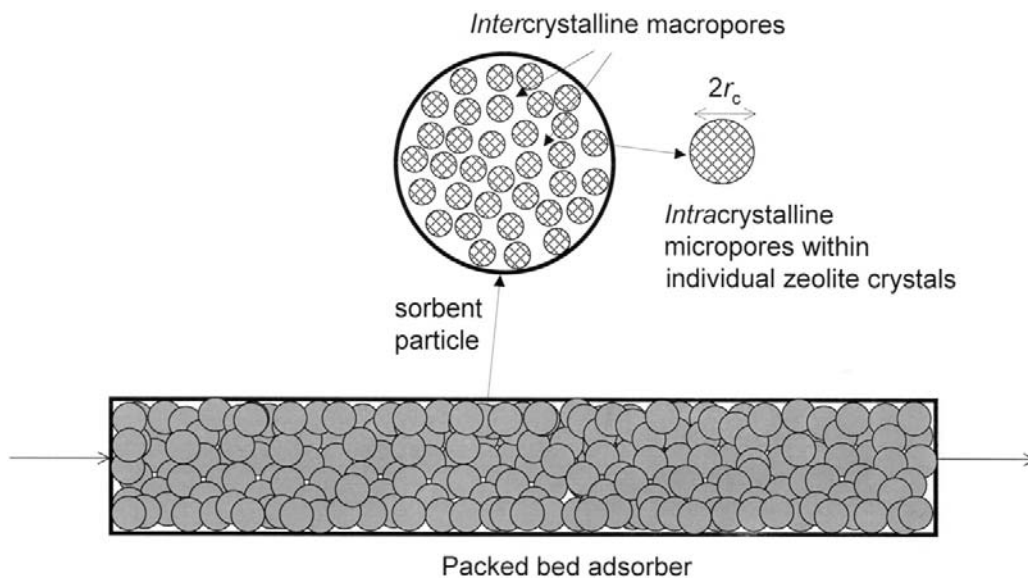
Fig. 22 Schematic of adsorbed packed with zeolite particles.

Table 4. As is conventional, we plot the normalized concentrations of the two components at the exit as a function of the dimensionless time tu_0/L where u_0 is the interstitial gas velocity at the inlet to the packed bed. In Fig. 23a the breakthrough curves with the Maxwell-Stefan model, with finite and infinite interchange coefficient $Ð_{ij}$, are compared. As expected, there are little differences in the two implementations of the Maxwell-Stefan model when the system approaches steady state. The major differences are during the initial transience. Finite interchange $Ð_{ij}$ tends to bring the breakthrough curves of O_2 and N_2 closer together; this is expected because of the slowing down of the

Table 4 Pure Component Langmuir Parameters and M-S Diffusivities for O_2 and N_2 in 4A Zeolite at 298 K

Factor	O_2	N_2
Saturation loading q_{sat} (mol kg^{-1})	9.54	6.68
Langmuir parameter, b (Pa^{-1})	4.95×10^{-8}	1.43×10^{-7}
$Ð_i$ (m^2 s^{-1})	1.438×10^{-14}	1.519×10^{-16}
Partial pressures at inlet to packed bed p (kPa)	63.8	240.2
Packed bed voidage ε (−)	0.4	
Length of bed, L (m)	0.6 m	
Interstitial gas velocity at inlet to bed, u_0 (m/s)	0.0436	
Crystallite radius, r_c (m)	1.3×10^{-6}	

Also given are the parameters of the packed bed.
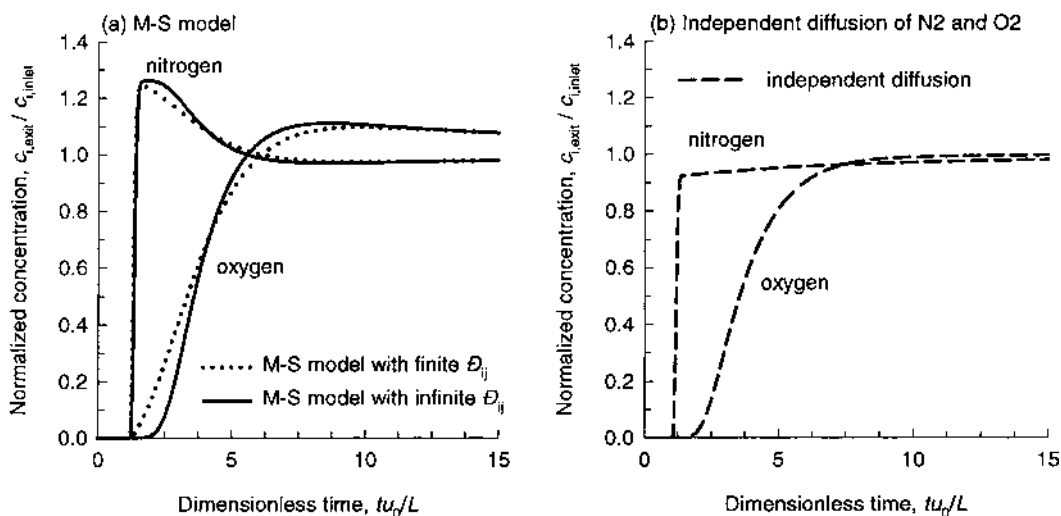*Source*: Data from Refs. 45 and 46.

Fig. 23 Breakthrough of N_2 and O_2 through packed bed of 4A zeolite particles. (a) Comparison of two implementations of the Maxwell-Stefan model, with finite and infinite interchange coefficient $Đ_{ij}$. The model parameters are specified in Table 4. (b) Breakthrough curves calculated using an independent diffusion model.

intracrystalline diffusion of O_2 and the concomitant speeding up of N_2. The slower diffusing N_2 exhibits a "roll-up" in both model implementations. For zeolite 4A, the Maxwell-Stefan implementation with $Đ_{ij} \rightarrow \infty$ is more appropriate. If each of the components were assumed to diffuse independently, oblivious of the other component with respect to both sorption *and* diffusion, the breakthrough behavior is shown in Fig. 23b; in this case, there is no roll-up of N_2. There is evidence in the literature (47) that a proper model of multicomponent mixture diffusion is essential for the success of this technology for air separation.

VI. CONCLUSIONS

The proper description of mixture sorption and diffusion is essential in applications of zeolites for separation and reaction. In this chapter we have focused on intracrystalline diffusion process. The following major points and conclusions emerge from the foregoing discussions.

1. Intracrystalline diffusion and sorption processes are intertwined; rigorous models are required to describe both phenomena.
2. *Ad*sorption and *de*sorption of single components proceed at significantly different rates.
3. The sorption isotherm of some types of molecules, e.g., branched alkanes in MFI, show inflection; this inflection behavior has a significant impact on the mixture sorption and diffusion.
4. For mixtures of molecules that differ in their saturation loadings, the proper description of the mixture isotherm requires the use of the IAST; the multicomponent Langmuir isotherm is inadequate in this case. Differences in

the saturation loadings lead to a size entropy effect that favors sorption of the smaller molecule.

5. The size entropy effect can have a significant impact on membrane permeation selectivity.

6. For sorption of mixtures of linear and branched alkanes in MFI, configurational entropy effects come into play; this causes the branched alkanes to be excluded from the zeolite. Configurational entropy effects can be exploited for achieving separations of alkane isomers.

7. The Maxwell-Stefan approach allows the prediction of mixture diffusion for some systems, on the basis of information on the pure component Maxwell-Stefan diffusivities, $Đ_i$, along with the mixture isotherms (estimated using say the IAST). The interchange coefficient $Đ_{ij}$ accounts for the slowing down of the molecule with the higher mobility, along with the speeding up of the molecule with the lower mobility.

8. In MFI zeolite, the complete Maxwell-Stefan model, with a finite interchange coefficient $Đ_{ij}$ calculated from Eq. (30) is required for proper description of mixture diffusion. This has been verified both from KMC simulations (34) and by comparison with experimental data on membrane permeation (24,26).

9. Published experimental data of Habgood (36) for uptake of N_2 and CH_4 in zeolite 4A is better simulated by the Maxwell-Stefan model in which the interchange occurs at an infinite rate, i.e., $Đ_{ij} \to \infty$.

10. There is a need for more experimental data on mixture diffusion in various zeolite structures in order to gain a better understanding of the influence of guest topology on the mixture diffusion characteristics.

11. Co- and counterdiffusion of binary mixtures are asymmetrical phenomena.

12. Accurate prediction of breakthrough behavior in a packed bed requires proper modeling of intracrystalline mixture diffusion.

NOMENCLATURE

A	surface area of adorbent, $m^2 \ kg^{-1}$
b_I	parameter in the Langmuir adsorption isotherm, Pa^{-1}
$[B]$	square matrix of inverse Maxwell-Stefan coefficients, $m^{-2} \ s$
c_I	molar concentration of species i, $mol \ m^{-3}$
D_i	Fick coefficient of pure component i, $m^2 \ s^{-1}$
D^*	self-diffusivity, $m^2 \ s^{-1}$
$[D]$	matrix of Fick diffusivities, m^2/s
$Đ_I$	Maxwell-Stefan diffusivity of species i in zeolite, m^2/s
$Đ_{ij}$	Maxwell-Stefan diffusivity describing interchange between i and j, m^2/s
f_I	fugacity of species i; $f_i = p_i$ for ideal gases, Pa
F	fractional approach to equilibrium, dimensionless
Fo	Fourier number, tD/r_c^2, dimensionless
k_B	Boltzmann constant, $1.38 \times 10^{-23} \ J \ molecule^{-1} \ K^{-1}$
L	length of packed bed, m
L_i	Onsgager coefficient of pure component i, $m^2 \ s^{-1}$
$[L]$	matrix of Onsgager coefficients, $m^2 \ s^{-1}$
m	summation parameter defined in Eq. (14), dimensionless
N_i	molar or molecular flux of species i, $mol \ m^{-2} \ s^{-1}$ or molecules $m^{-2} \ s^{-1}$

P	system pressure, Pa
P_i^0	vapor pressure analog in Eq. (36), Pa
p_i	partial pressure of species i, Pa
q_i	molar loading of component i, mol kg^{-1}
$q_{i,sat}$	saturation loading of component i, mol kg^{-1}
q_j	average loading of component i, mol kg^{-1}
r	radial distance coordinate, m
r_c	radius of spherical crystal, m
R	gas constant, 8.314 J mol^{-1} K^{-1}
Sh	Sherwood number, dimensionless
S	sorption selectivity defined by Eq. (35), dimensionless
S_P	permeation selectivity defined by Eq. (21), dimensionless
t	time, s
T	absolute temperature, K
u	abolute fluid velocity in packed bed, m s^{-1}
u_0	superficial fluid velocity in packed bed, m s^{-1}
x_i	mole fraction of component i in the adsorbed phase, dimensionless
y_i	mole fraction of component i in bulk vapour phase, dimensionless
z	distance coordinate along membrane, m

Greek Letters

δ	thickness of membrane, m
ε	porosity of packed bed, dimensionless
Γ	thermodynamic correction factor, dimensionless
$[\Gamma]$	matrix of thermodynamic factors, dimensionless
θ_i	fractional surface occupancy of component i
Θ_i	molecular loading, molecules per unit cell or per cage
$\Theta_{i,sat}$	saturation loading, molecules per unit cell or per cage
μ_i	molar chemical potential, J mol^{-1}
π	spreading pressure, Pa m
ρ	density, number of unit cells per m^3 or kg m^{-3}

Subscripts

A	referring to site A
B	referring to site B
1	component 1 in binary mixture
2	component 2 in binary mixture
mix	referring to mixture loading
sat	referring to saturation conditions
i,j	components in mixture
p	derivative at constant pressure
s	referring to surface of particle

Superscripts

0	pure component parameter

Vector and Matrix Notation

( )   component vector
[ ]   square matrix

REFERENCES

1. DM Ruthven. Principles of Adsorption and Adsorption Processes. New York: Wiley, 1984.
2. J Kärger, DM Ruthven. Diffusion in Zeolites and Other Microporous Solids. New York: Wiley, 1992.
3. DM Ruthven, S Farooq, KS Knaebel. Pressure Swing Adsorption. New York: VCH, 1994.
4. DM Ruthven, MFM Post. Diffusion in zeolite molecular sieves. In: H van Bekkum, EM Flanigan, PA Jacobs, and JC Jansen, eds. Introduction to Zeolite Science and Practice, 2nd ed. Studies in Surface Science and Catalysis Vol. 137. Amsterdam: Elsevier, 2001.
5. RT Yang. Gas Separation by Adsorption Processes. Boston: Butterworth, 1987.
6. DD Do. Adsorption Analysis: Equilibria and Kinetics. London: Imperial College Press, 1998.
7. NY Chen, TF Degnan, CM Smith. Molecular transport and reaction in zeolites. Design and application of shape selective catalysts, New York: VCH, 1994.
8. CJ Guo, O Talu, DT Hayhurst. Phase, transition and structural heterogeneity: benzene adsorption on silicalite. AIChE J 35:573–578, 1989.
9. DB Shah, CJ Guo, DT Hayhurst. Intracrystalline diffusion of benzene in silicalite: Effect of structural heterogeneity. J Chem Soc Faraday Trans 91:1143–1146, 1995.
10. EJ Maginn, AT Bell, DN Theodorou. Transport diffusivity of methane in silicalite from equilibrium and nonequilibrium simulations. J Phys Chem 97:4173–4181, 1993.
11. D Paschek, R Krishna. Monte Carlo simulations of self- and transport- diffusivities of 2-methylhexane in silicalite. Phys Chem Chem Phys 2:2389–2394, 2000.
12. DR Garg, DM Ruthven, The effect of the concentration dependence of diffusivity on zeolitic sorption curves. Chem Eng Sci 27, 417–423, 1972.
13. WE Schiesser. The Numerical Method of Lines: Integration of Partial Differential Equations. San Diego: Academic Press, 1991.
14. Z Du, G Manos, TJH Vlugt, B Smit. Molecular simulation of adsorption of short linear alkanes and their mixtures in silicalite. AIChE J 44:1756–1764, 1998.
15. TJH Vlugt, W Zhu, F Kapteijn, JA Moulijn, B Smit, R Krishna. Adsorption of linear and branched alkanes in the zeolite silicalite-1. J Am Chem Soc 120:5599–5600, 1998.
16. TJH Vlugt, R Krishna, B Smit. Molecular simulations of adsorption isotherms of linear and branched alkanes and their mixtures in silicalite. J Phys Chem B 103:1102–1118, 1999.
17. R Krishna, B Smit, TJH Vlugt. Sorption-induced diffusion-selective separation of hydrocarbon isomers using silicalite. J Phys Chem A 102:7727–7730, 1998.
18. R Krishna, D Paschek. Molecular simulations of adsorption and siting of light alkanes in silicalite-1. Phys Chem Chem Phys 3:453–462, 2001.
19. R Krishna, B Smit. Exploiting entropy to separate alkane isomers. Chem Innov 31(1):27–33, January 2001.
20. M Schenk, SL Vidal, TJH Vlugt, B Smit, R Krishna. Separation of alkane isomers by exploiting entropy effects during adsorption on silicalite-1: a configurational-bias Monte Carlo simulation study. Langmuir 17:1558–1570, 2001.

21. S Calero, B Smit, R Krishna, Separation of linear, mono-methyl and di-methyl alkanes in the 5–7 carbon atom range by exploiting configurational entropy effects during sorption on silicalite-1. Phys Chem Chem Phys **3**:4390–4398, 2001.
22. B Smit, TLM Maesen. Commensurate "freezing" of alkanes in the channels of a zeolite. Nature 374:42–44, 1995.
23. W Rudzinski, J Narkiewicz-Michalek, P Szabelski, AST Chiang. Adsorption of aromatics in zeolite ZSM-5: A thermodynamic-calorimetric study based on the model of adsorption and heterogeneous adsorption sites. Langmuir 13:1095–1103, 1997.
24. J Van de Graaf, F Kapteijn, JA Moulijn. Modeling permeation of binary mixtures through zeolite membranes. AIChE J 45:497–511, 1999.
25. JM van de Graaf, Permeation and separation properties of supported silicalite-1 membranes. Ph D dissertation. Delft University of Technology, 1999.
26. WJW Bakker. Structured systems in gas separation, Ph D dissertation. Delft University of Technology, 1999.
27. PH Nelson, M Tsapatsis, SM Auerbach. Modeling permeation through anisotropic zeolite membranes with nanoscopic defects. J Membrane Sci 184:245–255, 2001.
28. R Krishna, JA Wesselingh. The Maxwell-Stefan approach to mass transfer. Chem Eng Sci 52:861–911, 1997.
29. F Kapteijn, JA Moulijn, R Krishna. The generalized Maxwell-Stefan model for diffusion in zeolites: sorbate molecules with different saturation loadings. Chem Eng Sci 55:2923–2930, 2000.
30. R Krishna, D Paschek, Separation of hydrocarbon mixtures using zeolite membranes: a modelling approach combining molecular simulations with the Maxwell-Stefan theory. Sep Purif Technol 21:111–136, 2000.
31. FJ Keil, R Krishna, MO Coppens. Modeling of diffusion in zeolites. Rev Chem Eng 16:71–197, 2000.
32. D Paschek, R Krishna, Diffusion of binary mixtures in zeolites: kinetic Monte Carlo vs molecular dynamics simulations. Langmuir 17:247–254, 2001.
33. D Paschek, R Krishna. Inter-relation between self- and jump- diffusivities in zeolites. Chem Phys Lett 333:278–284, 2001.
34. D Paschek, R Krishna. Kinetic Monte Carlo Simulations of Transport Diffusivities of Binary Mixtures in Zeolites. Phys Chem Chem Phys 3:3185–3191, 2001.
35. N Sundaram, RT Yang. Binary diffusion of unequal sized molecules in zeolites. Chem Eng Sci 55:1747–1754, 2000.
36. HW Habgood. The kinetics of molecular sieve action. Sorption of nitrogen-methane mixtures by Linde molecular sieve 4A. Canad J Chem 36:1384–1397, 1958.
37. GF Round, HW Habgood, R Newton. A numerical analysis of surface diffusion in a binary adsorbed film. Separation Science 1:219–244. 1966.
38. AL Myers, JM Prausnitz. Thermodynamics of mixed gas adsorption, AIChE J 11:121–130, 1965.
39. HW Dandekar, GA Funk, HA Zinnen. Process for separating and recovering multimethyl-branched alkanes, US 6069289 to UOP, Inc. (2000).
40. HH Funke, AM Argo, JL Falconer, RM Noble. Separation of cyclic, branched, and linear hydrocarbon mixtures through silicalite membranes. Ind Eng Chem Res 36:137–143, 1997.
41. CJ Gump, RD Noble, JL Falconer. Separation of Hexane Isomers through Nonzeolite Pores in ZSM-5 Zeolite Membranes. Ind Eng Chem Res 38:2775–2781, 1999.
42. R Krishna, D Paschek. Permeation of hexane isomers across ZSM-5 zeolite membranes. Ind EngChem Res 39:2618–2622, 2000.
43. S Brandani, M Jama DM Ruthven. Counterdiffusion of p-xylene/benzene and p-xylene/o-xylene in silicalite studied by the zero-length column technique. Ind Eng Chem Res 39:821–828, 2000.
44. LJP Van den Broeke, R Krishna. Experimental verification of the Maxwell-Stefan theory for micropore diffusion. Chem Eng Sci 50:2507-2522, 1995.

45. S Farooq, DM Ruthven. Dynamics of kinetically controlled binary adsorption in a fixed bed. AIChE J 37:299–301, 1991.
46. OW Haas, A Kapoor, RT Yang. Confirmation of heavy-component rollup in diffusion-limited fixed-bed adsorption. AIChE J 34:1913–1915, 1988.
47. S Farooq, DM Ruthven. Numerical simulation of a kinetically controlled pressure swing adsorption process based on a diffusion model. Chem Eng Sci 46:2213–2224, 1991.